1971

Small angle tilt and twist grain boundary strengthening in yttrium

Thomas George Carnahan
Iowa State University

Small angle tilt and twist grain boundary strengthening in yttrium

by

Thomas George Carnahan

A Dissertation Submitted to the
Graduate Faculty in Partial Fulfillment of
The Requirements for the Degree of
DOCTOR OF PHILOSOPHY

Major Subject: Metallurgy

Approved:

Signature was redacted for privacy.

In Charge of Major Work

Signature was redacted for privacy.

For the Major Department

Signature was redacted for privacy.

For the Graduate College

Iowa State University
Ames, Iowa

1971

TABLE OF CONTENTS

I. INTRODUCTION

It has been known for over forty years that grain boundaries interfere with deformation (1-8). One noticeable result is that they strengthen metals. Surprisingly though only a small number of investigations into grain boundary strengthening have been undertaken. These investigations in one way or another were concerned with compatibility of deformation across grain boundaries. The earlier ones (9-14) were concerned with measuring the strengthening effect due to incompatibility and the later ones (15-25) were concerned with establishing experimentally the compatibility theories which had been derived earlier. All of these investigations were concerned with bicrystals containing large angles of misorientation when going from one component crystal to the other. The low angle of misorientation type of boundary has been almost completely neglected. For this reason, the experiments conducted in this investigation were limited almost exclusively to bicrystals containing small amounts of misorientation in going from one crystal to the other. A good theory based on dislocation arrays exists for grain boundaries of this type and it was hoped to discuss the observed strengthening effect in terms of dislocation theory.

A. Description of Experimental Program

The experiments of this study consisted of (a) a systematic determination of slip and twin modes of single crystal yttrium, (b) the effect of twist boundaries on the yield strength of bicrystals of yttrium, and (c) the measurement of the energy of twist boundaries in yttrium.

Part (a): The deformation of single crystals of yttrium in different orientations was necessary for two reasons. The first was to establish the deformation modes in yttrium which had never been unequivocally determined before. The second was that knowledge of the deformation modes was necessary in order to decide upon the best test orientation for the bicrystals containing twist boundaries which were used in the grain boundary strengthening experiments of part (b).

Part (b): The effect of twist boundaries on the yield strength of yttrium was an attempt to set up a simple enough experiment that would allow analysis of the observed strengthening effect due to grain boundaries to be discussed theoretically. The actual experiments were deformation of bicrystals in uniaxial compression whose halves were related to each other by a simple twist about an axis normal to a $\{10\bar{1}0\}$ plane. A plot of yield stress versus degree of twist mapped the strengthening effect.

Part (c): The measurement of twist boundary energies was used to provide an estimate of the dislocation structure

and content of the twist boundaries. Results of these experiments were used in conjunction with the strengthening effect data to discuss that data in terms of dislocation theory.

The rest of this introduction will be devoted to summarizing the existing pertinent information about single and bicrystal deformation experiments, discussing grain boundary energies, and establishing which forces arise due to the presence of the grain boundary in a bicrystal.

B. Single Crystal Deformation

Studies of the deformation of metals have shown that there are two means by which deformation can occur. One method involving the sliding of one layer of atoms over another is designated as slip, while the other method involving the cooperative movement of a large number of adjacent layers of atoms over one another is designated as twinning. In either case for a given metal there are only a small number of types of planes and types of directions in which deformation occurs.

It is known that slip occurs most easily on planes of the highest atomic density and in directions of the highest atomic density. These are designated close packed planes and close packed directions.

There does not seem to be any simple generalization for predicting twin planes and directions but the common twin

planes observed in metals are low index types.

1. Crystal structures of metals and their slip systems

In order to understand slip and twin modes it is necessary to group the common metals into three classes based on crystal structure. The three structures are face centered cubic (fcc), body centered cubic (bcc), and hexagonal close packed (hcp). Metals such as aluminum, copper, gold, silver, nickel, lead, platinum, and palladium are examples of face centered cubic metals. This group has a crystal structure built from unit cubes bearing one atom at each corner and one in the center of each face. The close packed planes are made up by the intersections of sets of three face diagonals which also are the close packed directions. These planes and these directions make up the slip systems in fcc metals. There are four equivalent slip planes and three equivalent slip directions per slip plane making a total of twelve equivalent slip systems. These systems are oriented so uniformly that a favorable slip system exists for all loading conditions. Figure 1a shows one of these slip systems.

Metals such as iron, niobium, vanadium, chromium, tantalum, and tungsten are examples of body centered cubic metals. This group has a crystal structure built from unit cubes bearing one atom at each corner and one in the center of the cube. There is no completely close packed plane so that the slip plane is not limited to just one specific type as for

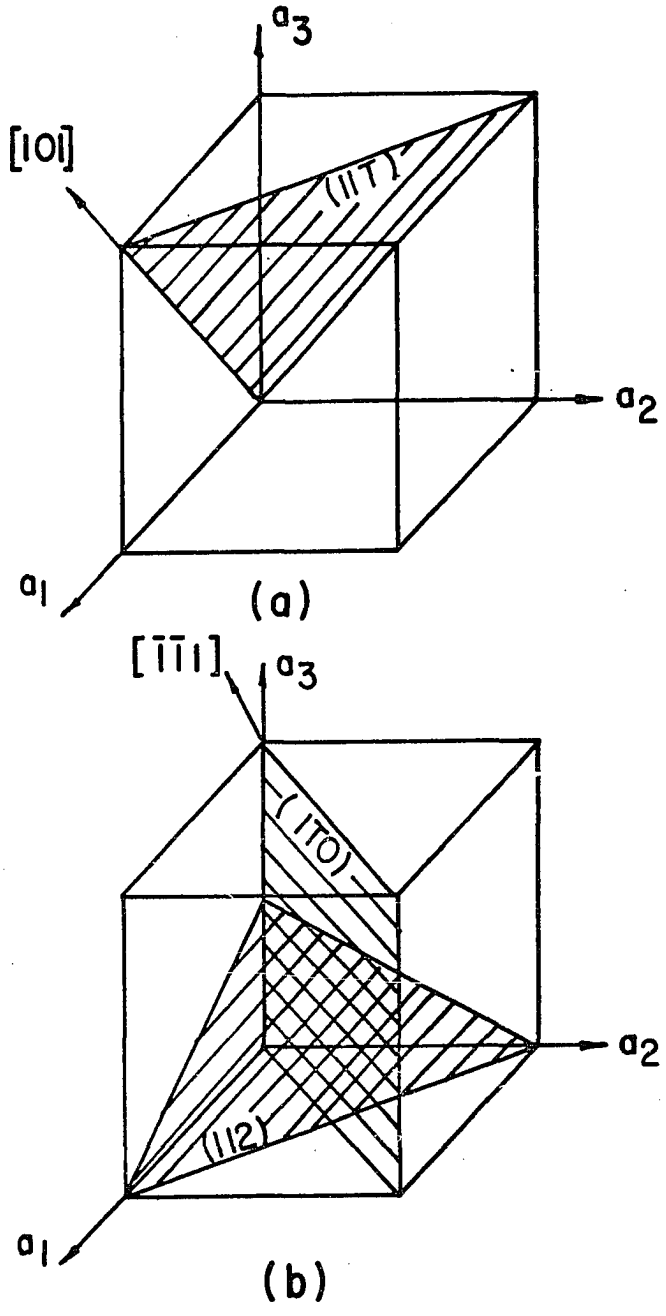

Figure 1. Slip systems in cubic metals. (a) $(11\bar{1})[101]$ slip in fcc. (b) $(1\bar{1}0)[\bar{1}\bar{1}1]$ and $(112)[\bar{1}\bar{1}1]$ slip in bcc

the fcc case. However, the diagonal of the cube is a close packed direction and is the observed slip direction. Here also there are enough slip systems to accommodate all loading conditions. Figure 1b shows two common types of bcc slip systems.

Metals such as zinc, cadmium, titanium, zirconium, yttrium, and beryllium are examples of hexagonal close packed metals. This group has a crystal structure built from a parallelepiped made from four equal rectangular faces and two equal rhombohedral ends whose included angles are 60° and 120°. An atom is placed at each corner and one is located half way between the ends and immediately over one of the triangles of atoms on an end. The more familiar hexagon shaped cell is made from three of these unit cells. If hcp atoms acted like spheres, there would be both a close packed plane (end of the parallelepiped) and close packed directions (formed by the intersection of the ends and sides of the parallelepiped). In reality, however, hcp unit cells are either slightly stretched or slightly flattened from the perfect sphere model. This causes one type of plane to be the most densely packed for the stretched cell and another type of plane to be the most densely packed for the flattened cell. The primary slip direction is the same for all hcp metals but secondary slip directions have been observed. Here in contrast to fcc and bcc systems the number and orien-

tation of slip systems is not favorable for slip under certain loading conditions so that twinning becomes an important deformation mode. Figure 2a shows a rarely observed slip system and Figure 2b shows examples of common hcp slip systems.

2. Crystallographic planes and directions

In order to easily identify planes and directions a set of coordinates and a method to locate the planes and directions is necessary. The three mutually perpendicular crystallographic directions for the case of cubic metals and the four crystallographic directions for the case of hcp metals form the coordinate systems for each crystal structure respectively. In all three systems the lattice constants a_1, a_2, a_3, and c act as unit vectors. In the case of directions a specific direction is set off by square brackets such as [w x y z] while a type of direction is set off by pointed brackets such as <w x y z>. In practice w is the number of a_1 lengths, x is the number of a_2 lengths, y is the number of a_3 lengths, and z (for the case of hcp only) is the number of c lengths parallel to their respective axes. In constructing a direction one end of the vector is fixed at the origin so all one has to do is move a point from the origin w lengths along the a_1 axis, then x lengths parallel to the a_2 axis, then y lengths parallel to the a_3 axis, and then z lengths (for hcp) parallel to the c axis and connect the origin to

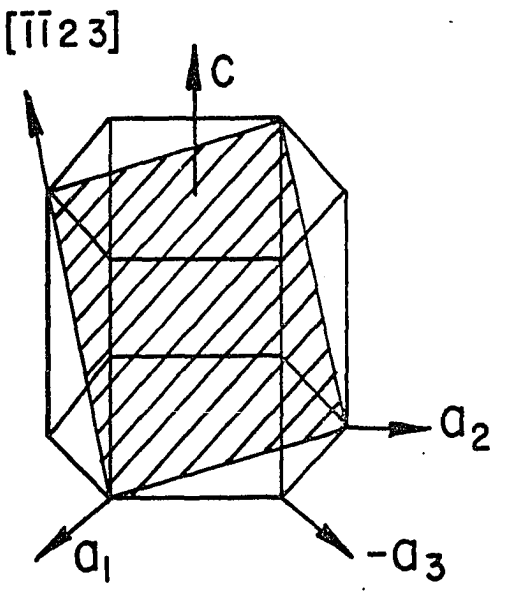

(a)

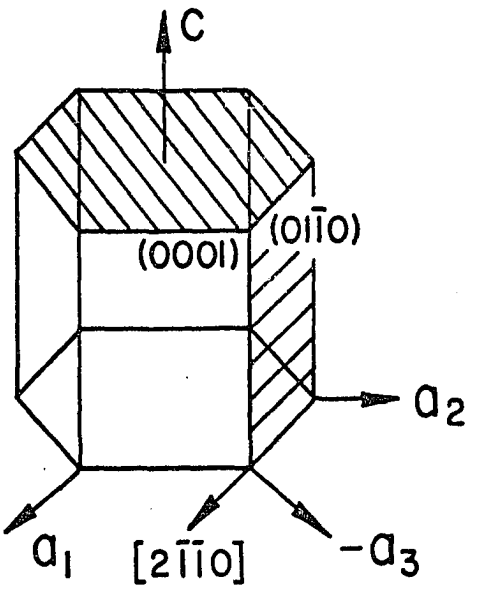

(b)

Figure 2. Slip systems in hcp metals. (a) $(11\bar{2}2)[\bar{1}\bar{1}23]$ slip system. (b) $(0001)[2\bar{1}\bar{1}0]$ and $(01\bar{1}0)[2110]$ slip systems

the point by a straight line.

The orientation of planes is denoted by a set of indices called Miller indices. The indices are simply a set of integers which are the inverse of the intersection in terms of fractions of lattice constants of the plane with each coordinate direction. The order of integers is the same as for directions. Specific planes are set off by parentheses such as (w x y z) while a family of planes is set off by curly brackets such as {w x y z}. As in the case of directions the four index notation is used only for the hcp case. To lay out a plane one makes each integer the denominator of a fraction whose numerator is 1 and places a point at 1/w along the a_1 axis, 1/x along the a_2 axis, 1/y along the a_3 axis, and (for hcp) 1/z along the c-axis. All of the points are coplanar thus establishing the desired plane.

3. Crystallography of twinning

While the deformation modes for fcc and bcc metals are basically slip mechanisms, the picture is not so clear for the case of hcp metals. As mentioned above these metals suffer from a lack of enough slip systems in certain orientations to permit deformation entirely by slip. Thus they usually twin when they are unfavorably oriented for slip. Twinning accomplishes two purposes. The first is the obvious one of allowing the metal to deform and the second is that the atom planes inside the twin are reoriented to a more favorable slip

orientation thereby permitting slip to take place within the twin.

In order to understand the crystallography of twinning the definition of a number of crystallographic elements is required. These are: a habit plane, K_1, which usually acts as the boundary between the twin and the matrix, an undistorted plane, K_2, a shear direction, n_1, and an undistorted direction, n_2. Another element called the plane of shear is perpendicular to K_1 and contains n_1. It also determines n_2 by its intersection with K_2. The shear angle, ϕ, is the acute angle between K_2 in the matrix and K_2 in the twin. These elements are shown in Figure 3b.

During the actual twinning process, K_2 moves from its original position through the shear angle ϕ to its final position. All vectors to the left of K_2 are shortened and all to the right are lengthened. Only those in K_2 are unaffected. This is shown in Figure 3a. Also, since a large number of planes shear over one another, the twin has a finite thickness, h, which is easily resolved in the optical microscope. The intersection of a twin with a free surface is also easily seen in the microscope because of the surface tilt it imparts. Therefore the amount and direction of shear may be determined by observing the intersection of a twin with free surfaces.

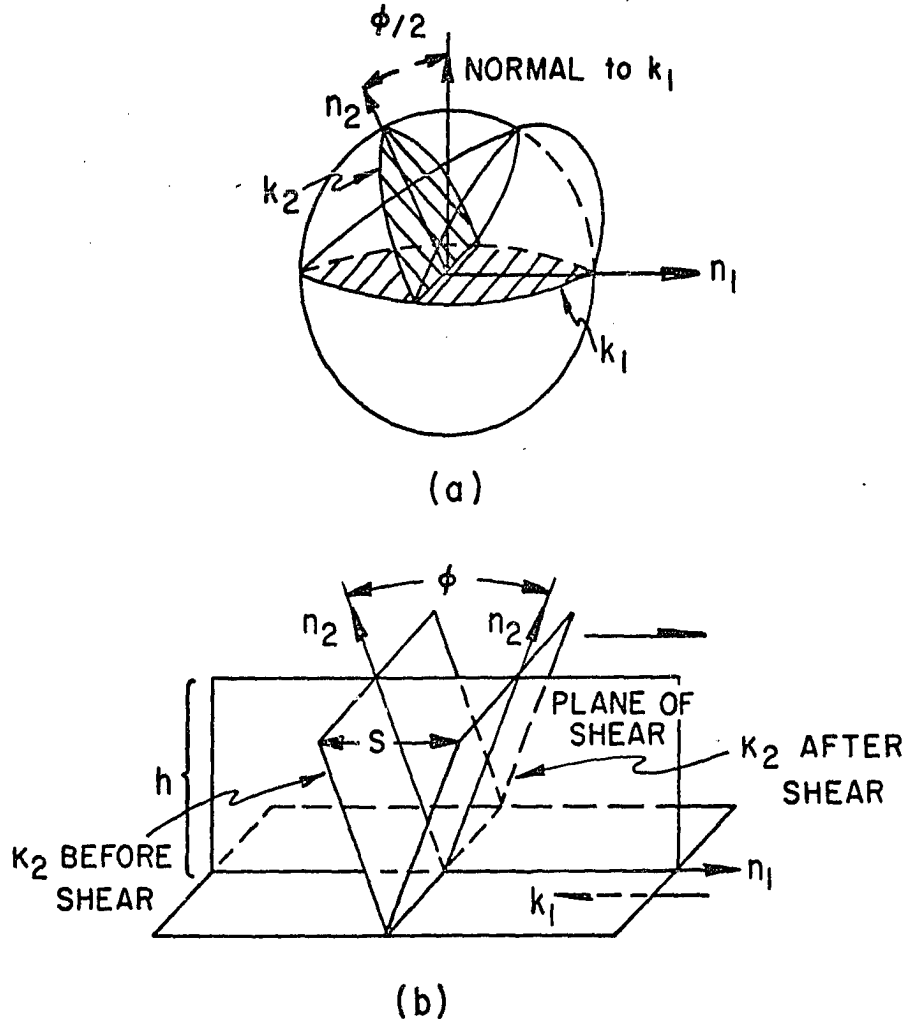

Figure 3. Illustrations of the crystallographic elements involved in twinning

4. Observed deformation modes in hcp metals

The hcp metals are divided into two groups when considering their deformation modes. The first group called high c/a ratio hcp metals consists of zinc and cadmium whose c/a ratios are 1.86 and 1.87 respectively. These are considerably larger than the 1.633 ratio for the case of packing of perfect spheres. The second group called low c/a ratio hcp metals consists of the rest of the hcp metals since their c/a ratios are less than 1.633. The low c/a ratio group has c/a ratios ranging from 1.57 for beryllium to 1.62 for magnesium. The two groups have quite different deformation modes and thus quite different deformabilities.

Table 1 summarizes the observed deformation modes of hcp metals. A glance at it shows that as a general rule low c/a ratio hcp metals deform by slip on the $\{10\bar{1}0\}\langle 1\bar{2}10\rangle$ slip systems and the high c/a ratio hcp metals deform by slip on the $(0001)\langle 11\bar{2}0\rangle$ slip systems. Beryllium, rhenium, magnesium and thallium are the exceptions to this rule.

A glance at the twin mode columns of Table 1 shows that high c/a ratio hcp metals show only $\{10\bar{1}2\}\langle 10\bar{1}1\rangle$ type twinning and low c/a ratio hcp metals usually show $\{11\bar{2}1\}\langle \bar{1}\bar{1}26\rangle$ primary twinning and usually $\{10\bar{1}2\}\langle \bar{1}011\rangle$ secondary twinning. The common twins in all cases belong either to the $\{10\bar{1}x\}$ zone or $\{11\bar{2}x\}$ zone. This is understandable because no primary slip systems operate near these orientations. Figure 4 shows

Table 1. Deformation modes observed in hcp metals

Metal	c/a	Slip modes Plane	Slip modes Direction	Twin modes K_1	Twin modes K_2	Twin modes n_1	Twin modes n_2	Reference
Cd	1.87	(0001)	$\langle 11\bar{2}0\rangle$	$\{10\bar{1}2\}$	$\{10\bar{1}\bar{2}\}$	$\langle 10\bar{1}\bar{1}\rangle$	$\langle 10\bar{1}1\rangle$	26,27
		$\{11\bar{2}2\}$	$\langle 11\bar{2}3\rangle$	-	-	-	-	
Zn	1.85	(0001)	$\langle 11\bar{2}0\rangle$	$\{10\bar{1}2\}$	$\{10\bar{1}\bar{2}\}$	$\langle 10\bar{1}\bar{1}\rangle$	$\langle 10\bar{1}1\rangle$	28,29,30
		$\{11\bar{2}2\}$	$\langle 11\bar{2}3\rangle$					31,32,33
Mg	1.62	(0001)	$\langle 11\bar{2}0\rangle$	$\{10\bar{1}2\}$	$\{10\bar{1}\bar{2}\}$	$\langle\bar{1}011\rangle$	$\langle 10\bar{1}1\rangle$	34,35,36
		$\{10\bar{1}0\}$	$\langle 1\bar{2}10\rangle$	$\{10\bar{1}1\}$	$\{10\bar{1}\bar{3}\}$	$\langle 10\bar{1}\bar{2}\rangle$	$\langle 30\bar{3}2\rangle$	37
		-	-	$\{10\bar{1}3\}$	$\{10\bar{1}1\}$	$\langle 30\bar{3}2\rangle$	$\langle 10\bar{1}\bar{2}\rangle$	
Re	1.62	(0001)	$\langle 11\bar{2}0\rangle$	$\{11\bar{2}1\}$	-	-	-	38
		$\{10\bar{1}0\}$	$\langle 1\bar{2}10\rangle$	$\{11\bar{2}2\}$	-	-	-	
		$\{10\bar{1}1\}$	$\langle 1\bar{2}10\rangle$	$\{10\bar{1}2\}$	-	-	-	
Tl	1.60	(0001)	$\langle 11\bar{2}0\rangle$	-	-	-	-	39
		$\{10\bar{1}0\}$	$\langle 1\bar{2}10\rangle$	-	-	-	-	
Hf	1.59	$\{10\bar{1}0\}$	$\langle 1\bar{2}10\rangle$	$\{10\bar{1}2\}$	$\{10\bar{1}\bar{2}\}$	$\langle\bar{1}011\rangle$	$\langle 10\bar{1}1\rangle$	40,41
		(0001)	$\langle 11\bar{2}0\rangle$	$\{11\bar{2}1\}$	-	-	-	
		$\{10\bar{1}1\}$	$\langle 1\bar{2}10\rangle$	-	-	-	-	
		$\{11\bar{2}2\}$	$\langle 11\bar{2}3\rangle$	-	-	-	-	

Table 1. (Continued)

Metal	c/a	Slip modes Plane	Slip modes Direction	Twin modes K_1	Twin modes K_2	Twin modes n_1	Twin modes n_2	Reference
Zr	1.59	$\{10\bar{1}0\}$	$\langle 1\bar{2}10\rangle$	$\{11\bar{2}1\}$	$\{11\bar{2}\bar{2}\bar{1}\bar{6}\}$	$\langle 11\bar{2}\bar{6}\rangle$	$\langle\bar{8}\bar{8}16\bar{3}\rangle$	41,42
		(0001)	$\langle 11\bar{2}0\rangle$	$\{11\bar{2}1\}$	(0001)	$\langle\bar{1}\bar{1}26\rangle$	$\langle 11\bar{2}0\rangle$	43,44
		$\{10\bar{1}1\}$	$\langle 1\bar{2}10\rangle$	$\{10\bar{1}2\}$	$\{10\bar{1}\bar{2}\}$	$\langle\bar{1}011\rangle$	$\langle 10\bar{1}1\rangle$	
		$\{11\bar{2}2\}$	$\langle 11\bar{2}3\rangle$	-	-	-	-	
Ti	1.59	$\{10\bar{1}0\}$	$\langle 1\bar{2}10\rangle$	$\{11\bar{2}1\}$	-	-	-	45,46,
		(0001)	$\langle 11\bar{2}0\rangle$	$\{10\bar{1}2\}$	-	-	-	47
		$\{10\bar{1}1\}$	$\langle 1\bar{2}10\rangle$	$\{11\bar{2}2\}$	-	-	-	
				$\{11\bar{2}3\}$	-	-	-	
				$\{11\bar{2}4\}$	-	-	-	
Gd	1.59	$\{10\bar{1}0\}$	$\langle 1\bar{2}10\rangle$	$\{11\bar{2}1\}$	-	-	-	40
		(0001)	$\langle 11\bar{2}0\rangle$	$\{10\bar{1}2\}$	-	-	-	
Dy	1.58	$\{10\bar{1}0\}$	$\langle 1\bar{2}10\rangle$	$\{11\bar{2}1\}$	-	-	-	40
		(0001)	$\langle 11\bar{2}0\rangle$	$\{10\bar{1}2\}$	-	-	-	
Ho	1.58	$\{10\bar{1}0\}$	$\langle 1\bar{2}10\rangle$	$\{11\bar{2}1\}$	-	-	-	40
		(0001)	$\langle 11\bar{2}0\rangle$	$\{10\bar{1}2\}$	-	-	-	

Table 1. (Continued)

Metal	c/a	Slip modes Plane	Slip modes Direction	Twin modes K_1	Twin modes K_2	Twin modes n_1	Twin modes n_2	Reference
Er	1.58	$\{10\bar{1}0\}$	$\langle 1\bar{2}10\rangle$	$\{11\bar{2}1\}$	-	-	-	40
		(0001)	$\langle 11\bar{2}0\rangle$	$\{10\bar{1}2\}$	-	-	-	
Y	1.57	$\{10\bar{1}0\}$	$\langle 1\bar{2}10\rangle$	$\{11\bar{2}1\}$	-	-	-	40,48
		(0001)	$\langle 11\bar{2}0\rangle$	$\{10\bar{1}2\}$	-	-	-	
				$\{11\bar{2}2\}$				
Be	1.57	(0001)	$\langle 11\bar{2}0\rangle$	$\{10\bar{1}2\}$	-	-	-	49,50
		$\{10\bar{1}0\}$	$\langle 1\bar{2}10\rangle$	-	-	-	-	

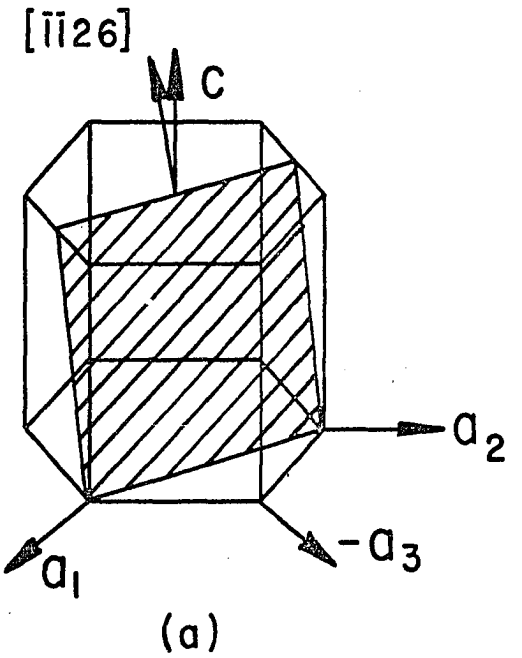

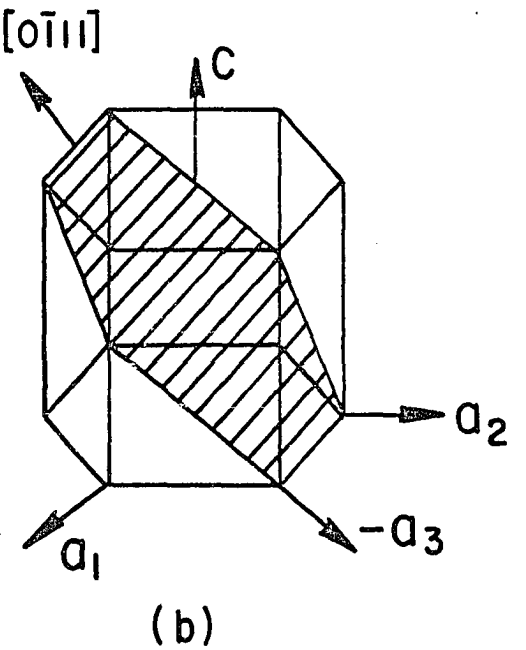

Figure 4. (a) $(11\bar{2}1)[\bar{1}\bar{1}26]$ twin, (b) $(01\bar{1}2)[0\bar{1}11]$ twin

examples of common hcp twins.

It is interesting to note that for low c/a ratio hcp metals when a sample is loaded in c-axis compression, of the commonly observed twins, only the $\{11\bar{2}2\}\langle 11\bar{2}\bar{3}\rangle$ twins should form. This is because there is no resolved shear stress on the ordinary $(0001)\langle 11\bar{2}0\rangle$ basal and $\{10\bar{1}0\}\langle 1\bar{2}10\rangle$ prism slip systems and the $\{11\bar{2}1\}\langle 11\bar{2}\bar{6}\rangle$ and $\{10\bar{1}2\}\langle\bar{1}011\rangle$ twin systems can only produce a net extension rather than contraction. This result occurs in titanium and zirconium but not in beryllium. Beryllium simply fractures when the load becomes high enough. No deformation occurs.

In summary high c/a ratio hcp metals deform mainly by slip on the $(0001)\langle 11\bar{2}0\rangle$ slip systems and twin on the $\{10\bar{1}2\}\langle 10\bar{1}\bar{1}\rangle$ twin systems. Low c/a ratio hcp metals deform mainly by slip on the $\{10\bar{1}0\}\langle 1\bar{2}10\rangle$ slip systems and twin on the $\{11\bar{2}1\}\langle 11\bar{2}\bar{6}\rangle$ and $\{10\bar{1}2\}\langle\bar{1}011\rangle$ systems. Deformation is mainly by slip but twinning assists by reorienting planes to more favorable slip orientations and by producing extension or contraction of the sample.

Yttrium is a low c/a ratio hcp metal so that on the basis of the above observations it would be expected to deform by $\{10\bar{1}0\}\langle 1\bar{2}10\rangle$ slip and by $\{11\bar{2}1\}\langle 11\bar{2}\bar{6}\rangle$ and $\{10\bar{1}2\}\langle\bar{1}011\rangle$ twinning. Two investigations have reported the deformation modes of yttrium. Rapperport and Hartley (48) studied the deformation modes by bending a large grained bar of yttrium. They

reported the slip planes to be $\{10\bar{1}0\}$ and (0001) planes and the twin planes to be $\{10\bar{1}2\}$, $\{11\bar{2}1\}$ and $\{11\bar{2}2\}$ planes. The (0001) and $\{11\bar{2}1\}$ planes were determined by one surface trace analysis and the other planes were determined by two surface trace analysis. Westlake (40) made the second study. He deformed a large crystal of yttrium and determined the slip planes to be the $\{10\bar{1}0\}$ planes and the twin planes to be of the $\{11\bar{2}1\}$ and $\{10\bar{1}2\}$ planes. These were all determined by two surface trace analysis. These two investigations showed that yttrium deforms by the same modes as the other low c/a ratio hcp metals but neither was complete in the sense of determining the slip directions or the other three twinning elements required for the complete solutions for the deformation modes. Also neither investigation studied the effect of temperature on the deformation modes or tested samples of controlled orientations.

C. Bicrystal Deformation

1. Compatibility of strain across the grain boundary

Practically all of the bicrystal deformation studies have turned out to deal with the problem of compatibility of strain across the grain boundary which can be thought of as the plane of abrupt orientation change of the slip system between two crystals. In most cases if the component crystals were not joined by the boundary but were placed in contact as though

they were joined and then deformed uniaxially the deformation would be such that the crystals would be displaced relative to one another at their junction. This is because their strains would not have been compatible across the junction. Had they been joined together by a grain boundary, the relative displacements could not have taken place. The effect of this would have been to force each component crystal to deform on other less favorable deformation systems in order to make the strain of each crystal at the boundary compatible. Livingston and Chalmers (15) were the first to treat this problem analytically. Their reasoning was as follows. Consider a bicrystal of square cross section subjected to uniaxial loading with the grain boundary parallel to a side and to the load axis as in Figure 5a. Let each crystal be oriented for single slip and call the left crystal A and the right crystal B. Let a coordinate system (X',Y',Z') be set up such that Z' coincides with the load axis and X' and Y' are normal to the side faces. Also define a coordinate system (X^i,Y^i,Z^i) for each crystal where the Z^i axis coincides with the slip plane normal and the Y^i coincides with the slip direction. The superscripts refer to either the A or B crystal. Let the crystal deform by a shear strain ϵ^i_{zy} in Y^i direction of each. Upon looking at the geometry of the bicrystals it can be seen that ϵ'^i_{xx}, ϵ'^i_{yy}, and ϵ'^i_{yx} are the only shear elements which describe the deformation of the grain

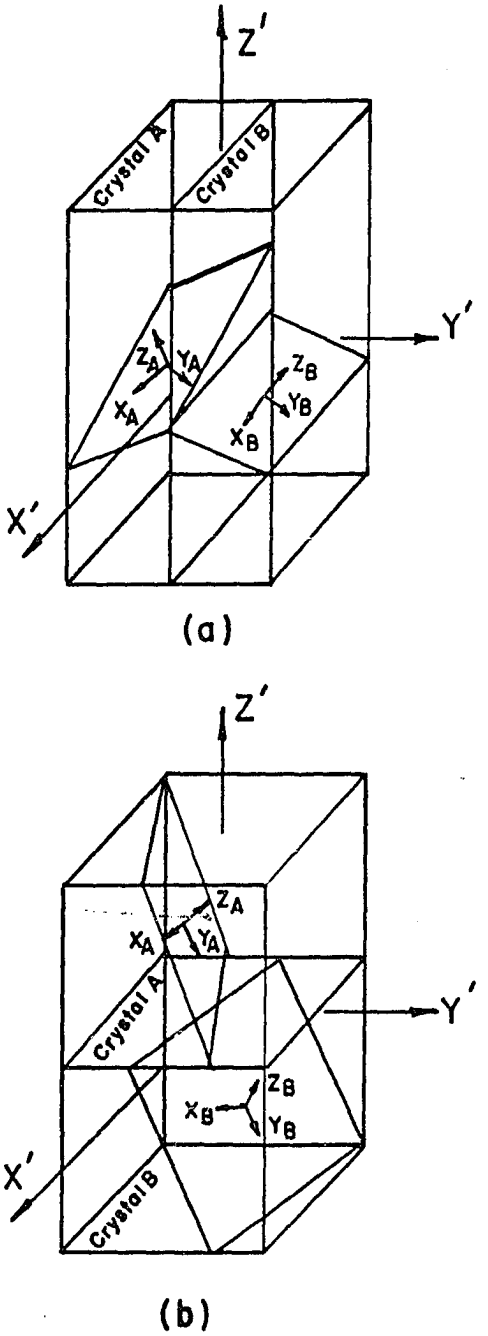

Figure 5. Geometries for compatibility of strain across the grain boundary in bicrystals. (a) Grain boundary parallel to load axis. (b) Grain boundary perpendicular to load axis

boundary in each crystal. It is next necessary to relate the ϵ^{i}_{zy} to the ϵ'^{i}_{xx}, ϵ'^{i}_{yy}, and ϵ'^{i}_{yx} by a tensor transformation which is of the general form

$$\epsilon'_{pq} = a_{pr}a_{qs}\epsilon_{rs}$$

where the first subscripts of the direction cosines, a_{pr} and a_{qs}, refer to the primed coordinate system and the second to the unprimed system. The transformed strains for the A crystal are

$$\epsilon'^{A}_{xx} = \cos(x';z^{A})\cos(x',y^{A})\epsilon^{A}_{zy} = m^{A}\epsilon^{A}_{zy}$$

$$\epsilon'^{A}_{yy} = \cos(y';z^{A})\cos(y';y^{A})\epsilon^{A}_{zy} = n^{A}\epsilon^{A}_{zy}$$

$$\epsilon'^{A}_{yx} = \tfrac{1}{2}[\cos(y';z^{A})\cos(x';y^{A})+\cos(x';z^{A})\cos(y';z^{A})]\epsilon^{A}_{zy} = p^{A}\epsilon^{A}_{zy}.$$

The equations for crystal B are

$$\epsilon'^{B}_{xx} = \cos(x';z^{B})\cos(x';y^{B})\epsilon^{B}_{zy} = m^{B}\epsilon^{B}_{zy}$$

$$\epsilon'^{B}_{yy} = \cos(y';z^{B})\cos(y';y^{B})\epsilon^{B}_{zy} = n^{B}\epsilon^{B}_{zy}$$

$$\epsilon'^{B}_{yx} = \tfrac{1}{2}[\cos(y';z^{B})\cos(x';y^{B})+\cos(x';z^{B})\cos(y';y^{B})]\epsilon^{B}_{zy} = p^{B}\epsilon^{B}_{zy}$$

However, when the deformation of the bicrystal is considered, a set of strain compatibility equations are necessary. These are

$$\epsilon'^{A}_{xx} = \epsilon'^{B}_{xx}$$

$$\epsilon'^{A}_{yy} = \epsilon'^{B}_{yy}$$

$$\epsilon'^{A}_{yx} = \epsilon'^{B}_{yx}$$

at the grain boundary. Therefore

$$m^{A}\epsilon^{A}_{zy} = m^{B}\epsilon^{B}_{zy}$$

$$n^{A}\epsilon^{A}_{zy} = n^{B}\epsilon^{B}_{zy}$$

$$p^{A}\epsilon^{A}_{zy} = p^{B}\epsilon^{B}_{zy}$$

or since the geometry of the situation requires for small strains that $\epsilon^{A}_{zy} = c\epsilon^{B}_{zy}$ then

$$m^{A} = cm^{B}$$

$$n^{A} = cn^{B}$$

$$p^{A} = cp^{B}.$$

For the case of an isoaxial bicrystal (one whose load axis is a direction common to each component crystal)

$$m^{A} = m^{B}$$

since the angles between the Z' axis and the slip planes and slip directions are fixed. However the requirements that

$$n^{A} = n^{B}$$

$$p^{A} = p^{B} \qquad (c = 1)$$

may or may not be satisfied. It turns out that for symmetric isoaxial bicrystals (those formed by rotation of each com-

ponent crystal equal amounts in opposite directions about the load axis) the above equality holds so that compatibility of strain across the grain boundary exists.

The result of the above analysis is that bicrystals which meet the compatibility criteria should only need one slip system on which to deform. Those that do not meet the criteria will require more slip systems and will force others to operate even though they may not be favorably oriented with respect to the external applied stress. This would tend to raise the yield stress.

2. Observations of grain boundary strengthening

Chalmers (9) was the first to perform deformation experiments on bicrystals. He measured the strengthening in bicrystals of tetragonal tin by testing nonsymmetric isoaxial tensile samples having the grain boundary parallel to the tension axis. They were pure tilt boundaries ranging from 0° to 90° tilt. The orientation was such that each [001] direction was 90° to the tensile axis and each [101] direction remained a constant 45° to the tensile axis. The bicrystals were formed by rotating each half about the tensile axis one half the tilt angle in opposite directions from each other. In this way the resolved shear stress remained constant for all angles of tilt and any increases in yield load of the bicrystals over single crystals was directly attributable to grain boundary strengthening. Chalmers found the strengthen-

ing to be a linear function of the amount of tilt; increasing from 0.400 Kg/mm^2 at 0° tilt to 0.640 Kg/mm^2 at 90° tilt.

Kawada (10) worked with asymmetric isoaxial large angle tilt boundaries in zinc bicrystals containing the grain boundaries parallel to the tensile axis. He fixed the orientation of the slip direction of one component crystal with respect to the grain boundary and varied the orientation of the slip direction of the other crystal from 0° to 315° tilt in increments of 45° tilt. In all cases the slip plane was oriented near 50° to the tensile axis in each half of the bicrystal. He followed this procedure for three sets of samples. The first set had the plane containing the slip direction and the tensile axis of the fixed half of the bicrystal at 90° to the plane of the grain boundary, the second set had the angle at 45°, and the third set had the angle at 0°. As in Chalmers case, the grain boundary strengthened the samples from a single crystal value of 0.30 Kg/mm^2 to 0.80 Kg/mm^2 for 130° misorientation. Unfortunately, Kawada's control of orientations was poor and little can be said about his results. One interesting result, though, was that for the symmetric isoaxial cases, the bicrystals behaved like single crystals. Gilman (11) observed this also in a symmetric non-isoaxial zinc bicrystal.

Clark and Chalmers (12) studied the deformation of non-symmetric nonisoaxial aluminum bicrystals containing tilt

boundaries. Their samples had the plane of the boundary parallel to the tensile axis. Single crystal seeds were made having the (111) plane oriented at 45° to the tensile axis and the $[1\bar{1}0]$ direction oriented at 45° to the tensile axis also. Bicrystals were then formed by rotating each seed in opposite directions about the [111] direction one half the total tilt angle. In this way the slip plane was continuous across the boundary and the slip direction varied in relation to the boundary. Since aluminum has no abrupt yield point, they extrapolated the initial linear work hardening region back to zero strain and defined the stress associated with it to be the yield stress. The results using this method of analysis showed the yield stress rising from 0.090 Kg/mm^2 at 0° tilt to 0.130 Kg/mm^2 at 20° tilt. The yield stress remained constant from 20° tilt to 75° tilt.

Aust and Chen (13) were the next to do yield stress measurements on bicrystals. They worked with symmetric isoaxial tensile samples of aluminum containing longitudinal boundaries. Their samples had the <110> direction parallel to the tensile axis. Tilt boundaries were formed by rotating each half about the <110> direction. Here the slip planes as well as the slip directions changed orientation abruptly upon crossing the grain boundary. They used the same method for determining yield stresses as Clark and Chalmers. Their plot of yield stress versus degree of tilt was a linear function

with stress increasing from 0.27 Kg/mm^2 at 0° tilt to 0.38 Kg/mm^2 at 90° tilt. Photomicrographs of slip lines showed slip line continuity across the 5° tilt boundaries but none at all for 85° tilt. Instead a region of multiple slip plane traces was seen near the grain boundary.

The results of the above investigations are summarized in Figure 6 and show that in nonsymmetric nonisoaxial bicrystals there is a general strength increase over single crystals with the strength increasing as the misorientation increases. Even symmetric isoaxial bicrystals show a strength increase so that macroscopic compatibility does not assure no strengthening. Also, nearly all the samples tested contained high angle boundaries so that dislocation interactions with the boundary could not be discussed easily.

Washburn (14) has been the only person to systematically study low angle boundary strengthening. He studied zinc samples containing either very low angle tilt boundaries or distributions of screw dislocations along (0001) planes. The tilt boundaries were formed along $\{11\bar{2}0\}$ planes and consisted of an array of parallel edge dislocations stacked one on top of the other. The screw distributions were formed by twisting a short length of crystal about the c-axis. This introduced screw dislocations along the (0001) planes in the twisted section. He found that the yield strength approached a maximum of about 50% above the single crystal value. This

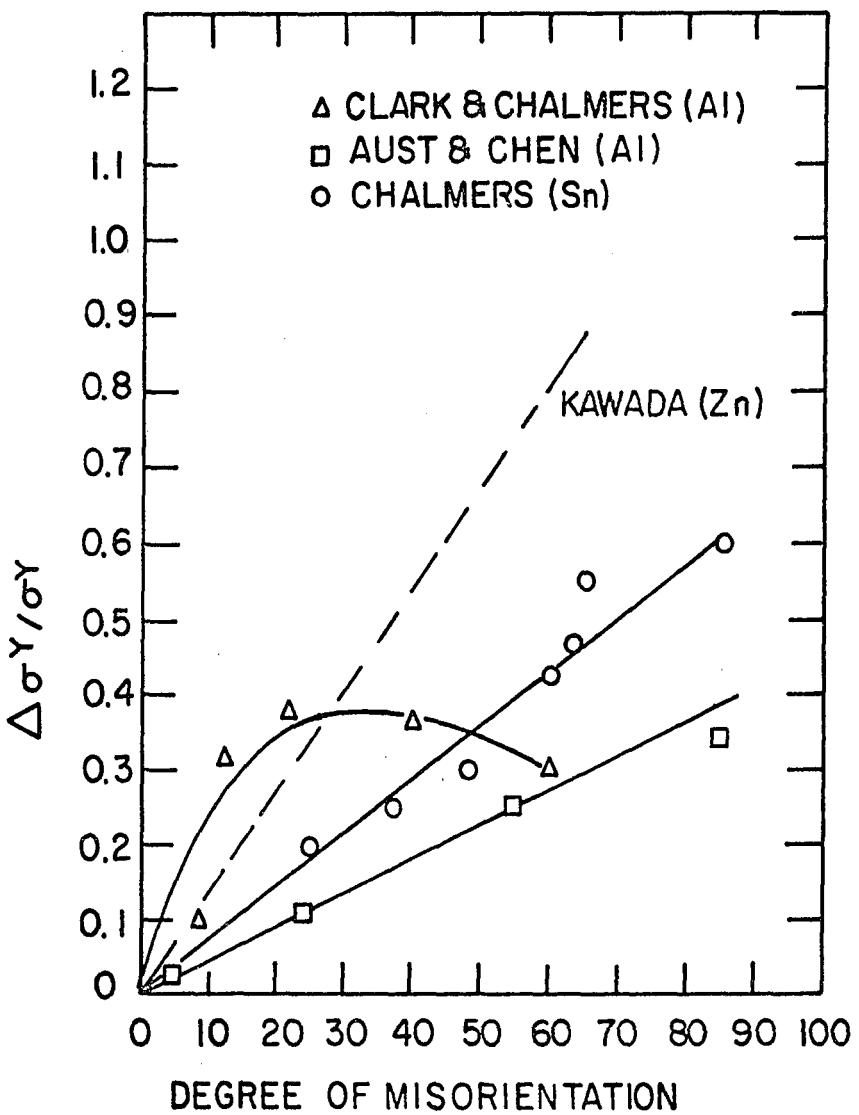

Figure 6. Summary of the strengthening effect observed in high angle incompatible bicrystals

occurred at about 1° of tilt or twist. All glide planes of the mobile dislocations were parallel to the glide planes of the boundary or array dislocations so that strengthening was probably due to the repulsive interaction of the stress fields of the glide dislocations and the boundaries or arrays.

The above discussion was a summary of all of the mechanical deformation experiments performed to measure the yield stress as a function of misorientation of the component crystals from one another. It showed that strengthening can take place due to the presence of high angle grain boundaries and is caused by the incompatibility of strain across the grain boundaries. Unfortunately only one set of experiments was run on small angle boundary samples and the results were over an extremely small range of misorientations. No one has ever studied the strengthening caused by small angle boundaries over the full range of misorientations. It was for this purpose that the experiments on small angle boundary strengthening performed here were run.

3. Dislocations and small angle boundaries

The concept of the dislocation is now a necessary element to be added to the discussion since small angle boundaries are considered to be made up of arrays of dislocations. Dislocations are line imperfections in crystals and were originally postulated to explain the large magnitude difference between theoretical and actual yield strengths in crystals.

There are two types of dislocations which are called edge and screw respectively. An edge dislocation can be thought of as an extra half plane of atoms in a crystal. This extra half plane moves through the crystal when the applied stress is at least as great as the yield strength. When it passes completely out of the crystal, a step appears on the surface due to the shear. The displacement vector, called the Burgers vector, is the magnitude of the step. It can be seen from Figure 7b that the Burgers vector lies in the slip plane and is perpendicular to the extra half plane.

The screw dislocation, as seen in Figure 7a, is much harder to visualize but is easiest to think of as a spiral ramp of atoms running through the crystal. It moves perpendicular to its axis. The Burgers vector is determined by the step formed in going from any point on the ramp to the corresponding point 360° asround the axis of the ramp. Here the Burgers vector is parallel to the dislocation line.

It can be seen that it is possible for the Burgers vector to point in one of two directions while in actuality it only points in one direction. This problem is resolved by defining a vector called a tangent vector which is tangent to the dislocation as implied by its name. The direction of the Burgers vector is then defined by the closure failure occurring when going equal numbers of steps in each direction clockwise around the core of the dislocation while sighting

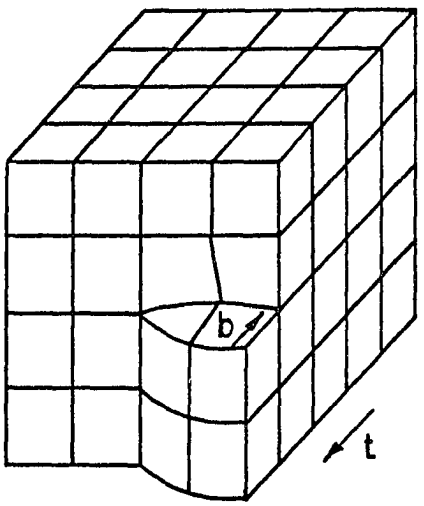

(a)

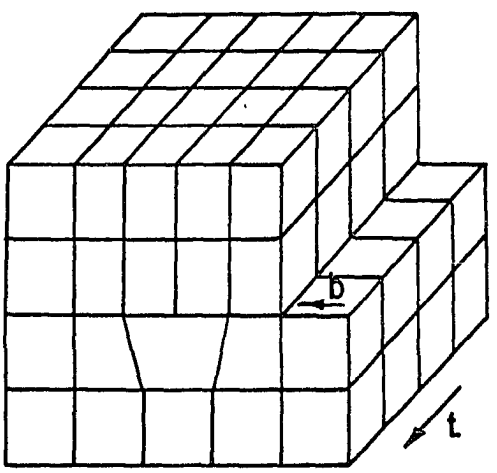

(b)

Figure 7. Models for dislocations. (a) Screw dislocation. (b) Edge dislocation

down the positive direction of the tangent vector. The Burgers vector connects the finish point to the start point of the Burgers circuit. A typical Burgers circuit is illustrated for an edge dislocation in Figure 8a. Figure 8b and Figure 8c show the tangent and Burgers vectors for a right handed screw and a positive edge dislocation respectively located parallel to the Z axis of a set of coordinates.

When groups of parallel dislocations are arranged in planes they can cause a small orientation change from one side of the array to the other side. These are known as small angle boundaries. Two small angle boundary dislocation models have been postulated; one for tilt and one for twist boundaries. The tilt boundary is simply a wall of parallel edge dislocations one above the other while the twist boundary is made from a grid of two perpendicular arrays of parallel screw dislocations. Amelinckx and Dekeyser (51) have shown that these arrays are stable and that the stress fields die out within a short distance from the boundary. These are two necessary criteria for a valid boundary to exist in a crystal.

A simple tilt boundary may be visualized as having been formed by cutting out a wedge of crystal whose tip angle is the tilt angle and bringing the two surfaces into contact with each other. This is illustrated in Figure 9. The misorientation angle, θ, is defined by

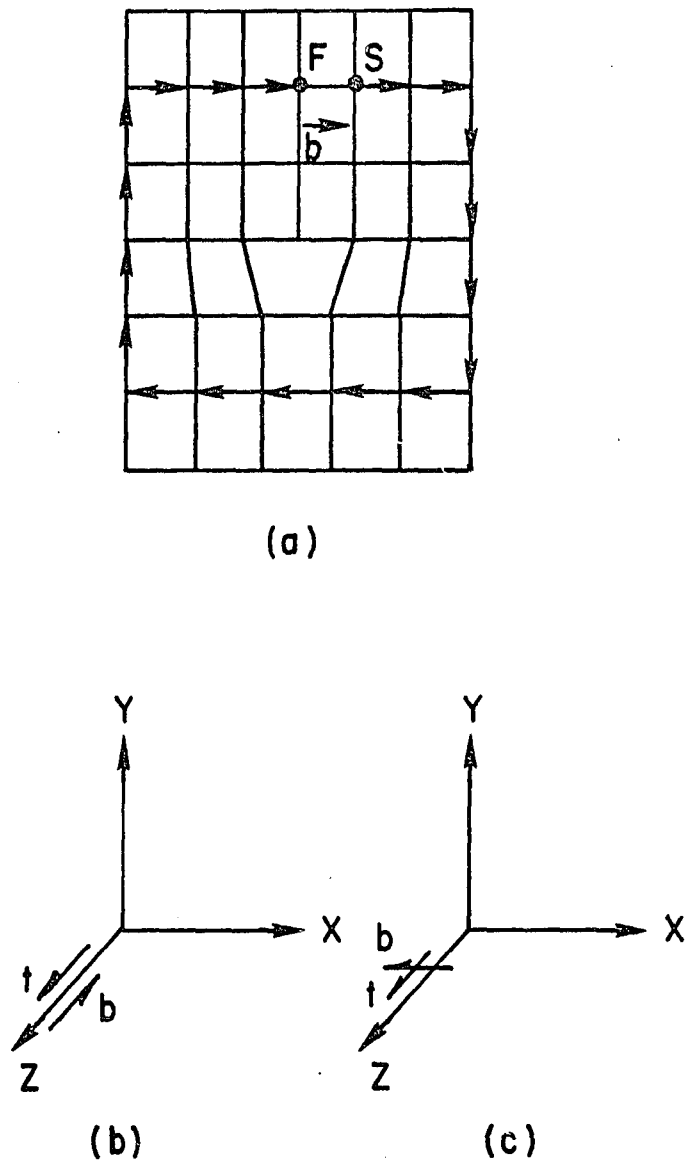

(a) Burgers circuit around an edge dislocation. The tangent vector points into the plane of the paper. (b) Tangent and Burgers vectors for a right hand screw dislocation oriented along Z axis. (c) Tangent and Burgers vectors for a positive edge dislocation oriented along Z axis

Figure 8. Tangent and Burger's vectors of dislocation

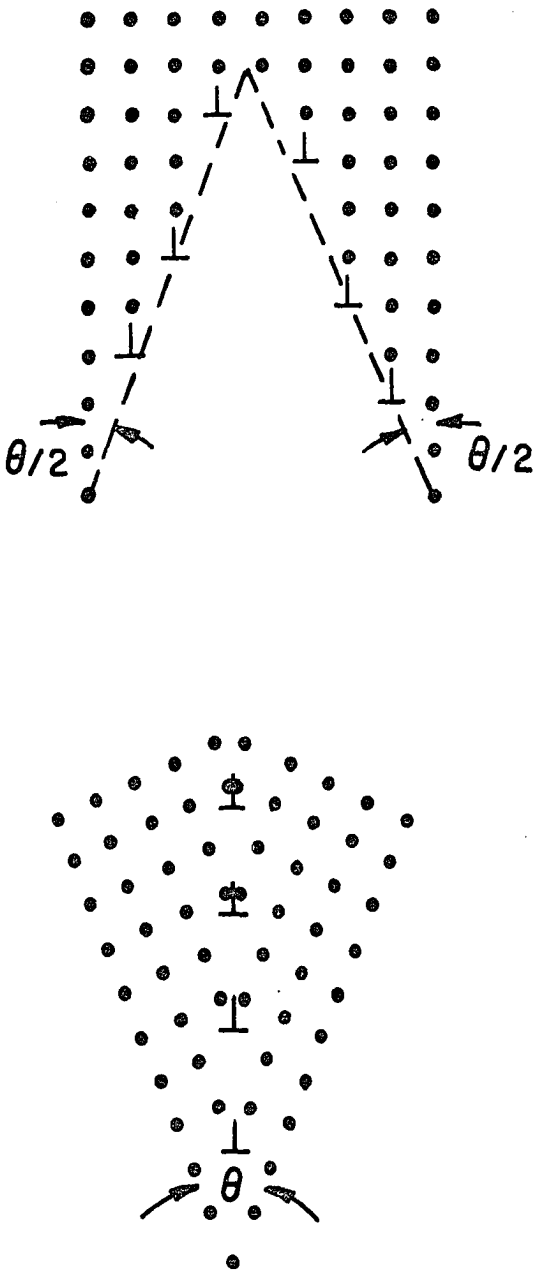

Figure 9. Model illustrating the formation of a tilt grain boundary

$$\text{Tan } \theta = nb/H.$$

The separation, h, between dislocations of the boundary is

$$h = b/2\sin(\theta/2) \approx b/\theta \qquad (1)$$

for small θ. The dislocation density, 1/h, is

$$1/h = \theta/b.$$

The simple twist boundary is visualized as having been formed by the superposition of two sets of parallel screw dislocation arrays at right angles to each other. This is illustrated in Figure 10. For each array

$$\text{Tan } \theta = n_i b_i/H_i \qquad \text{where } i = 1, 2.$$

The separation, h_i, is

$$h_i = H_i/n_i = n_i b_i/n_i \text{Tan}\theta \approx b_i/\theta$$

for small θ.

The dislocation density, $1/h_i$, is

$$1/h_i = 1/h_1 + 1/h_2 = \theta/b_1 + \theta/b_2 = \theta(b_1+b_2)/b_1 b_2.$$

It can be seen that for both twist and tilt boundaries the dislocation density increases until the cores begin to overlap. This is usually from 4° to 9° misorientation. Once core overlap occurs the concept of the dislocation boundary is replaced by a disordered transition zone of atoms concept.

There is a limited amount of direct experimental evidence for the above boundary structures but in all cases the concepts developed above were verified. Amelinckx (52) reviewed early decoration techniques used to reveal boundary structure,

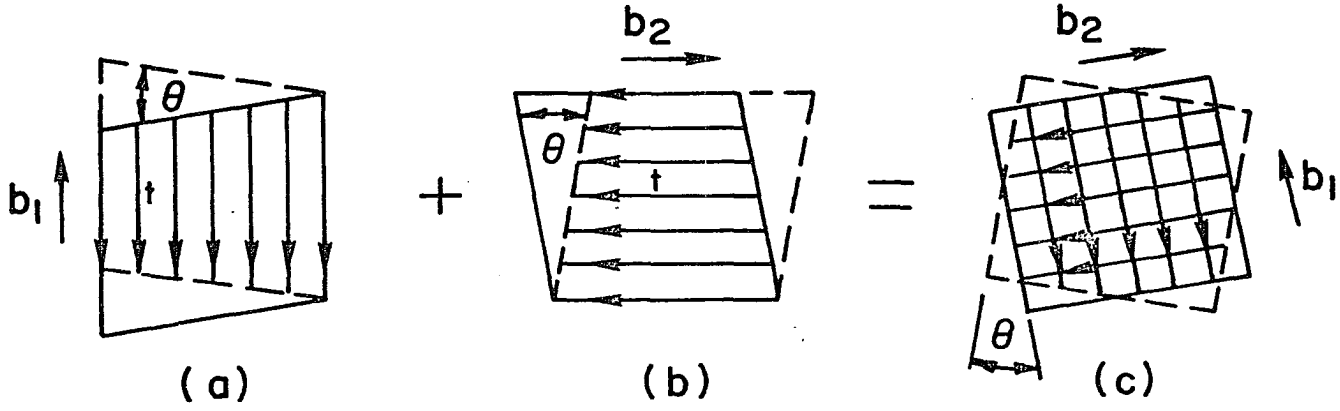

Figure 10. Model illustrating the formation of a twist grain boundary by the superposition of two perpendicular arrays of parallel screw dislocations

Vogel (53) studied the structure of low angle boundaries in germanium by etch pit techniques and Schober and Balluffi (54,55) studied [001] twist boundaries in gold foils by transmission electron microscopy. These last three studies also verified the equations for the dislocation spacing as a function of misorientation, θ.

In summary, a small angle boundary is seen to be composed of an array of dislocations whose stress field is short range in nature and the resultant Burgers vectors produce the proper orientation change in going from one crystal to the next. Two special types of dislocation boundaries were considered. The first was the symmetric tilt boundary. Symmetric tilt boundaries were shown to be made up of parallel edge dislocations stacked one above the other. The second boundary considered was the symmetric twist boundary. Symmetric twist boundaries were shown to be made up of two perpendicular sets of parallel screw dislocations. The dislocation density was shown to increase with increasing misorientation until core overlap occurs. At that point the concept of individual dislocations broke down and was replaced by a disordered transition zone of atoms concept.

4. Small angle grain boundary energy-Read-Shockley theory

Dislocations possess a self energy so that a dislocation boundary being composed of an array of dislocations will possess an energy. This energy will be a measure of the dis-

location density of the boundary and thus of the dislocation spacing. Therefore, an experiment whereby the energy of the grain boundary is measured will give a measure of the dislocation spacing. If this measurement is made as a function of the amount of tilt or twist, a specific model for the dislocation spacing as a function of the amount of tilt or twist will be verified. Once the dislocation structure of the boundary is known the forces exerted on glide dislocations by the boundary as a function of misorientation can be calculated and compared with the strengthening effect observed from stress-strain tests on bicrystals of the same misorientations. Read and Shockley (56) derived the theory of small angle dislocation boundary energies and Gjostein and Rhines (57) verified it by measuring the energies of tilt and twist boundaries of copper as a function of misorientation. The variation of the grain boundary energy as a function of the misorientation is given by

$$E = E_o\theta[A-\ln\theta]$$

where

$$E_o = \frac{\mu b}{4\pi(1-\nu)}$$

$$A = \frac{4\pi(1-\nu)E_c}{\mu b^2}$$

for tilt boundaries and

$$E_o = \frac{\mu b}{2\pi} ,$$

$$A = \frac{2\pi}{\mu b^2} E_c$$

for twist boundaries. The symbols in the above equations are:

b = burgers vector

ν = poissons ratio

μ = shear modulus

E_c = core energy of the dislocation

In actual practice the energy equation is converted to a relative energy equation by dividing by the surface energy, γ^s.

$$R_\gamma = E/\gamma^s$$

$$R_o = E_o/\gamma^s$$

so that the energy equation is converted to

$$R_\gamma = R_o\theta[A-\ln\theta].$$

Dividing by θ gives the final working expression.

$$R_\gamma/\theta = R_o[A-\ln\theta] \qquad (2)$$

A plot of R_γ/θ versus $\ln\theta$ should then give a straight line if the data follows the Read-Shockley theory. The slope will be $-R_o$ and the intercept will be R_oA so that values of E_o and E_c can be computed if the surface energy is known or the surface energy can be computed if the values of b, μ, and ν are known.

5. Forces caused by the grain boundary in a bicrystal

There are seven possible forces which can arise due to the presence of the grain boundary in a bicrystal. These are

due to

1. Incompatibility of strain across the grain boundary.
2. A change in shear modulus from one component crystal to the other.
3. A change in the force law between the atoms in the extension of the slip plane of one crystal into the other.
4. The interaction of the stress field of the grain boundary with the stress field of the glide dislocations.
5. The formation of attractive dislocation junctions.
6. The formation of jogs in the glide dislocations and in the dislocations forming the grain boundary as the glide dislocations pass through the boundary.
7. The dragging of jogged segments of the glide dislocations after intersection with the grain boundary.

The first force, which is due to incompatibility of strain across the grain boundary, has already been described and discussed.

The second force, which arises due to a change in the shear modulus when going from one crystal to the other, is a long range image force (58). It can arise for the case of a composite material of two different shear moduli and actually has been observed for the case of metals covered by oxide layers (59) since the shear modulus of oxides is usually much

higher than for metals.

The third force, arising due to a change in the force law between the atoms in the extension of the slip plane of one crystal into the other, is based on the fact that the extension of the slip plane must require a larger shear stress to allow slip since it is not the observed slip plane. The geometry of the situation is shown in Figure 11. Jaswon and Foreman (60) have calculated the force due to this mechanism. They assumed the force law to be the Peierls force in the crystal containing the slip plane and Hookes law in the extension of the slip plane crystal. The Hookes law assumption is valid until the dislocation core approaches the boundary. Then the Hookes law assumption breaks down and a repulsive force arises. The force calculated by Jaswon and Foreman is equal to

$$\frac{\mu b^4}{96\pi^2(1-\nu)^4 S^4}$$

where S is the distance of the dislocation from the grain boundary.

The last four forces arise due to dislocation interactions. The first of these is the interaction of glide dislocations with the stress field of the grain boundary. This is essentially the interaction of the individual dislocations of the boundary with the glide dislocation since the stress field of the boundary is short range in nature. Amelinckx

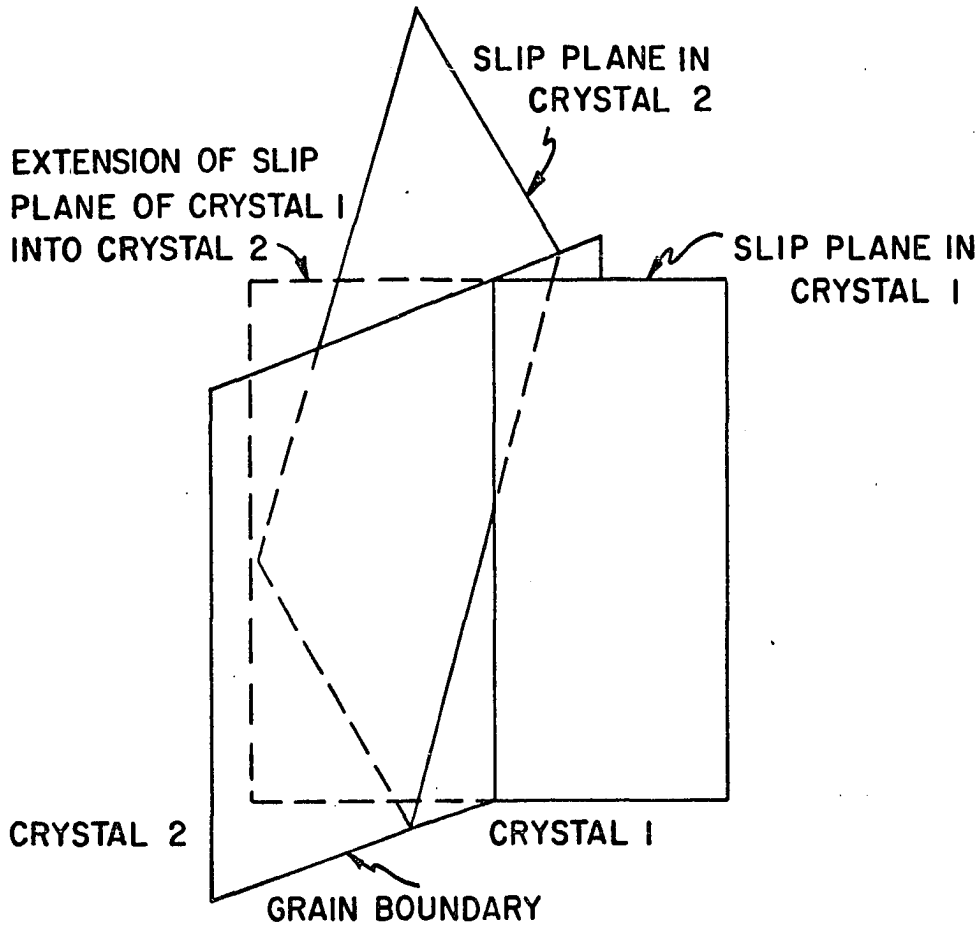

Figure 11. Model illustrating the extension of a slip plane of one component crystal of a bicrystal into the other component crystal

and Dekeyser (51) show that a large repulsive stress can arise for a glide dislocation parallel to and in the same slip plane as one of the dislocations forming the boundary. This was probably the strengthening mechanism in Washburn's experiments on zinc bicrystals.

The force arising due to the formation of attractive dislocation junctions occurs when the glide dislocation intersects the boundary dislocations at some angle (61). There is a junction formed at each crossing point and if the glide and boundary dislocations can combine to form a short length of a third dislocation with a resulting energy decrease an attractive junction is formed. The force needed to dissociate the junction causes an overall strengthening in the bicrystal.

The force arising due to formation of jogs in the glide and boundary dislocations arises when the glide dislocation intersects the boundary dislocations at some angle as in the case of attractive junctions. The formation of jogs requires energy so an additional force must be applied to provide this energy.

Once the jogs have been formed they will have to glide on a plane that is not necessarily one of the normal glide planes. This will give rise to the last force, a jog dragging force, since the nonnormal glide plane has a higher resolved shear stress for glide than the normal one. Also,

for screw dislocations the jog will have to move nonconservatively i.e. by climb. This would cause a very large strengthening force for this special case.

The last four forces would tend to increase with increasing misorientation since the dislocation density increases with increasing misorientation. This is in agreement with Washburn's work on zinc.

II. MATERIALS

Two grades of yttrium were used in the experiments performed in this investigation. A commercial purity grade that had been electron beam melted to reduce fluorides was used to determine the single crystal growth techniques. It was also used for most of the deformation mode and grain boundary energy experiments. A high purity grade of yttrium was used for all of the bicrystal deformation studies and some of the grain boundary energy and deformation mode studies. The major impurity in both grades, oxygen, was at a level of 3730 ppm in the commercial purity grade and 750 ppm in the high purity grade. It is interesting to note that yttrium oxide precipitates in commercial purity yttrium were easily resolved at 200X magnification. They were star shaped plates which lay parallel to the (0001) planes.

Yttrium is extremely hard to fabricate so that both grades were extruded to rod from cylindrical billets. The commercial purity grade was coated with graphite and extruded from a 5.0 cm diameter to a 1.90 cm diameter rod at 400°C. The high purity grade was sealed in a titanium can which in turn was sealed inside a copper can and extruded at 400°C. The copper can was necessary to bring the billet diameter up to the size of the tooling of the extrusion press. The copper-titanium skin was machined off and all residual

titanium was dissolved off in a 50% HNO_3-50% HF acid solution. The final diameter of the high purity rod was 1.57 cm.

Table 2 presents the chemical analysis in ppm by weight of the yttrium used in this investigation.

Table 2. Chemical analysis of yttrium

Impurity	C	O	N	H	F	Ca	Cr	Cu
Comm. purity	359	3730	176	4	20	d<10	20	50
High purity	50	752	11	2	9.4	d<10	20	10

Impurity	Fe	Mg	Ni	Si	Ta	Ti	Zr	W
Comm. purity	100	d<10	>500	50	-<200	>500	-	-<200
High purity	200	d<10	60	300	700	80	-	-

III. EXPERIMENTAL PROCEDURE AND RESULTS

A. Single Crystal Deformation

1. Production of large yttrium single crystals

Single crystals of metals may be produced by solidification from the melt or by solid state grain growth techniques. Yttrium single crystals must be produced by the second method since a high temperature phase transformation (62) interferes with the solidification method. Of all the solid state techniques tried, the one that worked was a twenty-four hour 1673°K vacuum anneal of sections of as-extruded rod. This temperature was just below the phase transition temperature. The method must have depended upon the unique structure of the as-extruded material because samples from arc-melted material, while exhibiting large grains, never had grains that grew entirely through their cross sections. The cooling rate was not critical. Most rods were cooled to room temperature within an hour of the termination of the anneal. The starting material was short rods of yttrium about 4.0 cm long by 1.57 cm diameter. After the anneal the rods contained from one to four crystals along their lengths. Most of the grain boundaries were perpendicular to the axis of the rod. This resulted in the rod containing the so called "bamboo" grain structure. The grains were usually related to each other by a twist about the rod axis with the (0001) plane being nearly

parallel to the axis and the grain boundary being nearly a $\{10\bar{1}0\}$ plane.

2. Preparation and testing of deformation mode samples

The complete crystallographic description of a deformation mode requires the determination of the plane and direction of deformation. The most unambiguous method of determining the deformation plane is to follow the trace of the particular mode of interest on two intersecting flat faces of a single crystal of known orientation. This is known as the two surface trace analysis technique (63). Measurement of the angles on each face that the trace makes with the common edge supplies enough information when combined with the orientation of the faces to determine the indices of the plane. This procedure can be applied to either slip plane or twin plane determination.

The determination of deformation directions usually requires a different technique for slip than for twinning because the amount of shear corresponding to a given slip line is much less than for a twin. Furthermore, the shear angle of the twin must also be determined. The slip direction is determined by observing the relative amounts of displacement on each of two surfaces. This may be done for the case of coarse slip by observing the displacement of interference fringes across a deformation band in an interference microscope. Fine slip requires either a scanning electron micro-

scope or electron microscope replica techniques. A technique for determining the deformation direction directly is to find the orientation where no surface relief is observed at all. This is parallel to the deformation direction. It may be done quite conveniently for slip in cylindrical single crystals by rotating the deformed crystal about its axis until the slip lines disappear.

As mentioned above twin deformation direction determination requires knowledge of the amount of shear as well as the direction of shear so that its analysis is a little different than for slip. Here instead of measuring the amount of surface relief on each of two surfaces, the angle through which the surface of the twin has been tilted with respect to the parent surface is measured for each of two surfaces (64). These data are then resolved into one half the shear angle, $\emptyset/2$, and the direction of shear, n_1. Knowledge of these values and the twin plane are sufficient for the complete twin solution. The surface tilt may be determined by X-ray or interference microscopy techniques.

The techniques used for slip mode determination in these experiments were two surface trace analysis for the determination of the slip planes and a modification of the slip line disappearance method described for cylindrical crystals. The modification was required because the samples used were of square cross section. It owed its success to the previous

data which indicated that the slip direction lies in the (0001) plane. The samples were made with the (0001) plane parallel to the compression axis. If the slip direction lay in the (0001) plane, no slip lines would be observed on that face after deformation and the thickness between those faces would remain constant. These facts coupled with two surface analysis of slip lines on the other vertical face and the compression face would be enough to establish the slip direction.

Twin mode determinations were as described above with interference microscopy being the main tool for the shear determinations. Figure 12b shows an interference micrograph of a $\{10\bar{1}0\}$ face of yttrium. The abrupt change in continuity is due to the surface tilt of a $\{10\bar{1}2\}$ $\langle\bar{1}011\rangle$ twin. The tilt was determined by measuring the width of the twin and the displacement of the interference fringes from one side of the twin to the other side.

The samples used in these studies were of various shapes. Deformation mode samples were mainly compression samples but one was pulled in tension and one was bent. The compression samples were rectangular parallelepipeds, the tensile sample a solid cylinder, and the bend test sample a small rectangular plate.

The compression samples were spark cut into four orientations. These and the axes of the applied loads are shown in Figure 13. The first orientation (Figure 13a) had the com-

Figure 12. Typical interference micrographs
(a) Interference micrograph of a 5.5^{o} twist grain boundary thermal groove
(b) Interference micrograph of the tilt of a $\{10\bar{1}0\}$ surface due to a $\{10\bar{1}2\}$ twin

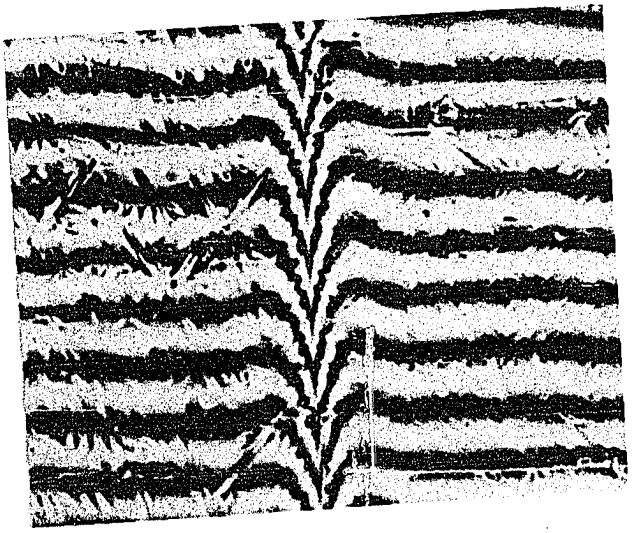

a

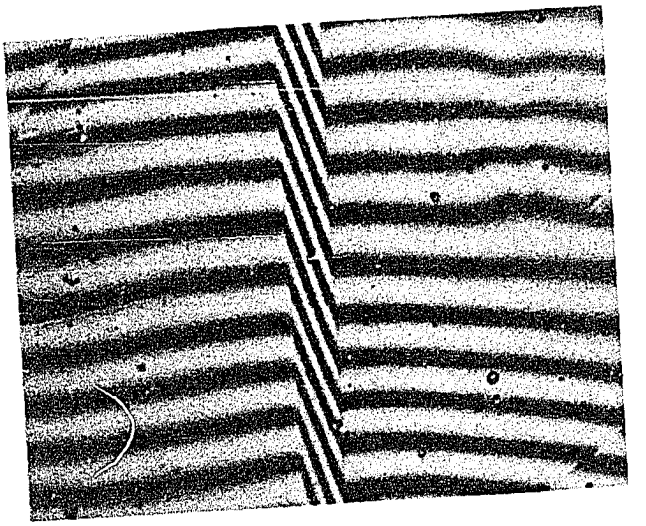

b

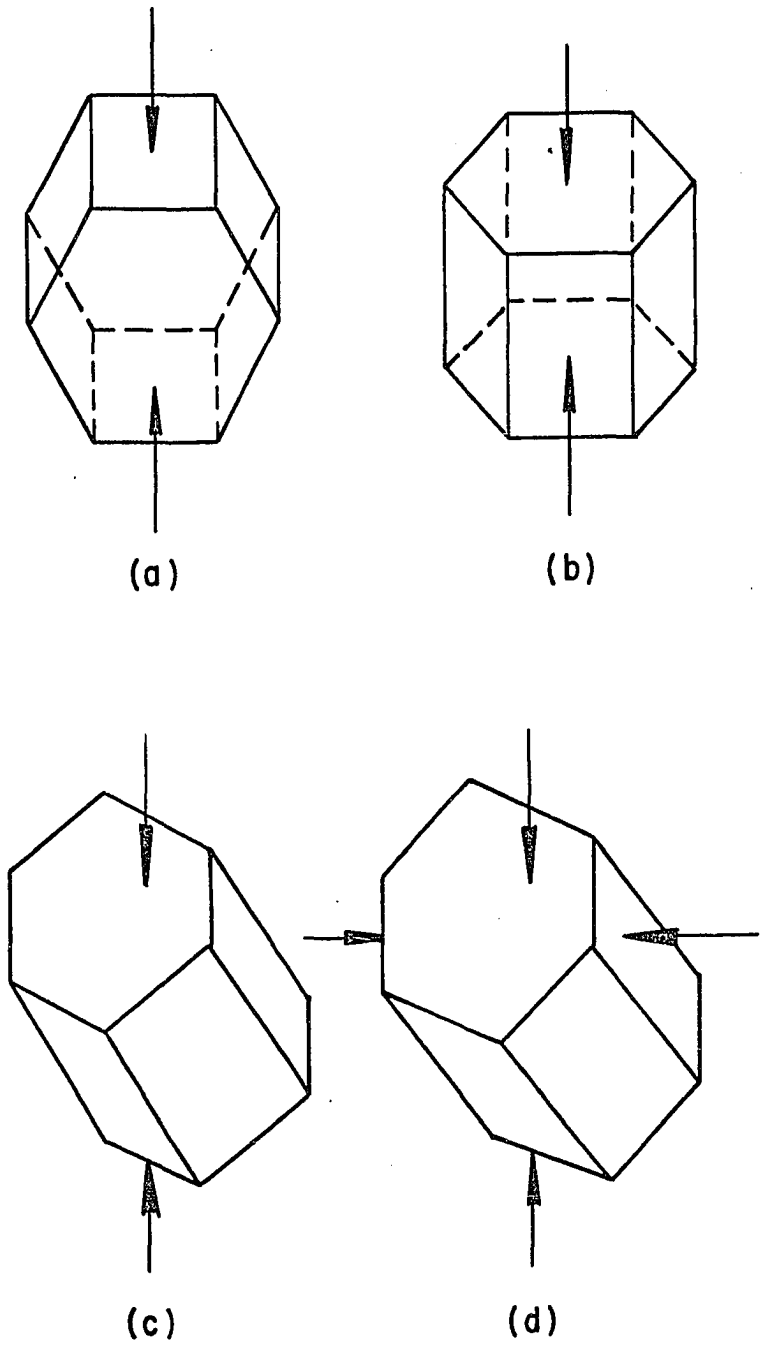

Figure 13. Loading schemes used in deformation mode study (a) $\langle 10\bar{1}0 \rangle$ axis compression, (b) c-axis compression, (c) $\langle 11\bar{2}2 \rangle$ axis compression, (d) plane strain compression

pression axis parallel to a $\langle 10\bar{1}0\rangle$ direction. The ends were then $\{10\bar{1}0\}$ planes and the sides were (0001) and $\{\bar{1}2\bar{1}0\}$ planes. This orientation resolved no stress on the (0001) $\langle 11\bar{2}0\rangle$ basal slip system but was well oriented for $\{10\bar{1}0\}$ $\langle\bar{1}2\bar{1}0\rangle$ slip.

The second compression orientation (Figure 13b) had the $\langle\bar{1}2\bar{1}2\rangle$ direction as the compressive axis. These samples had an irrational plane for ends and the $\{10\bar{1}0\}$ and $\{\bar{1}2\bar{1}3\}$ planes for sides. This orientation was ideal for (0001)$\langle 11\bar{2}0\rangle$ slip and also for $\{11\bar{2}1\}\langle\bar{1}1\bar{2}6\rangle$ twinning.

The third compression orientation (Figure 13c) had the c-axis as the compression direction. Here the only deformation mode expected to operate was $\{11\bar{2}2\}\langle 11\bar{2}\bar{3}\rangle$ twinning. Neither the (0001)$\langle 1120\rangle$ slip system nor the $\{10\bar{1}0\}\langle\bar{1}2\bar{1}0\rangle$ slip system had any stress resolved on them. Also the $\{10\bar{1}2\}$ $\langle 10\bar{1}1\rangle$ twins and the $\{11\bar{2}1\}\langle\bar{1}\bar{1}26\rangle$ twins could not operate because they could only produce a net extension in that orientation. This orientation was suitable to check for non-basal slip directions as well as $\{11\bar{2}2\}\langle 11\bar{2}\bar{3}\rangle$ twinning.

The fourth compression orientation (Figure 13d) was a plane strain orientation to favor basal slip and retard twinning. Here the compression axis was located 40° from the c-axis and the sidewall restraint force was perpendicular to an a-axis.

The tensile sample was a c-axis sample. Here both

$\{10\bar{1}2\}\langle\bar{1}011\rangle$ twinning and $\{11\bar{2}1\}\langle\bar{1}\bar{1}26\rangle$ twinning were expected because the sample could elongate. No slip modes were expected for the reasons given for the c-axis compression case.

The bend test sample had the $\{10\bar{1}0\}$ plane as the plane that was bent i.e. parallel to the neutral plane. The curved side face was a $\{1\bar{2}10\}$ plane and the undisturbed side face was the (0001) plane.

The compression samples of the first three orientations were tested at 77°K, 298°K and 497°K. The tensile, plane strain and bend test samples were tested only at 298°K. The low and high temperature tests were run while the sample and compression rig were submerged in a constant temperature bath of liquid nitrogen or hot silicone oil. The temperature of the silicone oil bath was maintained constant to within $\pm$ 2°K for the duration of any test by an on-off controller. Low temperatures were measured by a copper-constantan thermocouple and high temperatures were measured by a mercury thermometer. All tests were given a twenty minute temperature equilibration period before the actual loading began. A 0.007 cm thick Teflon film protected the ends of the samples in contact with the compression platens. This worked so well that slip lines could be observed on these faces.

All samples were spark cut from a larger single crystal which had been mounted on a three circle goniometer and oriented by the Laue back reflection X-ray technique. The

orientation of the cut surfaces was within 2° of the desired orientation.

Once the samples had been spark cut, they were mounted in a jig which allowed hand lapping of the spark cut surfaces without altering the orientation of the faces. A short electropolish in a 6% perchloric acid-94% methanol electrolyte maintained at 193°K removed the worked surface due to lapping. Each crystal was identified and all three dimensions were measured with a micrometer. The samples measured about 0.30 x 0.30 x 0.60 cm with the long dimension being the gage length. All samples were tested at a cross head rate of 0.0127 cm/min. in an Instron machine. Load-elongation curves monitored the stress-strain characteristics of each type of orientation.

3. Results and discussion of deformation mode experiments

Table 3 summarizes the results of the experiments performed in this investigation. It can be seen from Table 3 that the common slip mode is $\{10\bar{1}0\}\langle 1\bar{2}10\rangle$ prism slip. Quite unusual conditions such as plane strain loading are required before $(0001)\langle 11\bar{2}0\rangle$ basal slip becomes active. The primary twin is the $\{11\bar{2}1\}\langle \bar{1}\bar{1}26\rangle$ type since it was observed in all loading situations excluding c-axis compression where it could not operate. The $\{10\bar{1}2\}\langle \bar{1}011\rangle$ twin is the secondary twin since it was the primary twin only in c-axis tension but was not seen in some of the other loading situations. The

Table 3. Deformation modes of yttrium

Stress axis	Slip modes		Twin modes K_1	K_2	n_1	n_2	ϕ_{obs}	ϕ_{theo}
<10$\bar{1}$0>comp.	{10$\bar{1}$0}	<1$\bar{2}$10>	{11$\bar{2}$1}	(0001)	<$\bar{1}\bar{1}$26>	<11$\bar{2}$0>	-	-
<0001>comp.	-	-	{11$\bar{2}$1}	(0001)	<$\bar{1}\bar{1}$26>	<11$\bar{2}$0>[a]	-	-
<11$\bar{2}$3>comp.	-	-	{11$\bar{2}$1}	(0001)	<$\bar{1}\bar{1}$26>	<11$\bar{2}$0>	-	-
<0001>tension	-	-	{10$\bar{1}$2}	{10$\bar{1}\bar{2}$}	<$\bar{1}$011>	<10$\bar{1}$1>	-	-
<0001>tension	-	-	{11$\bar{2}$1}	(0001)	<$\bar{1}\bar{1}$26>	<11$\bar{2}$0>	-	-
plane strain comp.	(0001)	<11$\bar{2}$0>	{11$\bar{2}$1}	(0001)	<$\bar{1}\bar{1}$26>	<11$\bar{2}$0>	-	-
plane strain comp.	{10$\bar{1}$0}	<1$\bar{2}$10>	{10$\bar{1}$2}	{10$\bar{1}\bar{2}$}	<$\bar{1}$011>	<10$\bar{1}$1>	-	-
<10$\bar{1}$0>bend test	{10$\bar{1}$0}	<1$\bar{2}$10>	{11$\bar{2}$1}	(0001)	<$\bar{1}\bar{1}$26>	<11$\bar{2}$0>	38.0°	35.30°
<10$\bar{1}$0>bend test	-	-	{10$\bar{1}$2}	{10$\bar{1}\bar{2}$}	<$\bar{1}$011>	<10$\bar{1}$1>	11.2°	11.16°

[a]Only observed in local region where sample contacted compression platens.

$\{11\bar{2}2\}\langle 11\bar{2}\bar{3}\rangle$ twin which was reported by Rapperport and Hartley (48) was not observed in these tests even though it was the only deformation mode favored in c-axis compression. There is no reason for this discrepancy unless the very low shear angle (1.34°) could somehow have been affected by the different impurity levels present in the two lots of yttrium.

No deformation modes other than the $\{11\bar{2}1\}\langle\bar{1}\bar{1}26\rangle$ twins mentioned in Table 3 were observed in c-axis compression. The sample simply fractured along a plane oriented 46° from the basal plane. This is shown in the two photographs of a fractured c-axis sample in Figure 14. The fracture plane for this sample intersected the $\{11\bar{2}0\}$ face parallel to the intersection of that face with the (0001) face. This fact along with the 46° orientation with respect to the (0001) plane made the fracture plane a $\{11\bar{2}3\}$ plane. The $\{11\bar{2}3\}$ fracture plane and the lack of any deformation modes in c-axis compression probably account for the poor fabricability of yttrium. Also the lack of any deformation modes in c-axis compression shows conclusively that no pyramidal slip of non-basal Burgers vector operates in yttrium.

Slip was extremely fine in both commercial and high purity yttrium. Figure 15a shows $\{10\bar{1}0\}\langle 1\bar{2}10\rangle$ slip at a magnification of 1400X. The lines are parallel and straight. Figure 15b shows both $\{10\bar{1}0\}\langle 1\bar{2}10\rangle$ slip and $(0001)\langle 11\bar{2}0\rangle$ slip in the plane strain compression sample at 400X. This is quite

Figure 14. Photographs of fractures c-axis compression sample. (a) Overview of the fractured sample. The front face is a $\{11\bar{2}0\}$ plane and the fracture plane is a $\{11\bar{2}3\}$ plane. (b) View normal to $\{1\bar{2}10\}$ face. 5X magnification

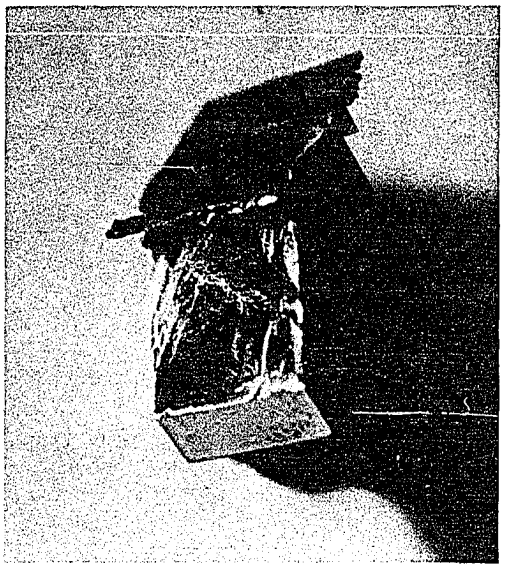

a

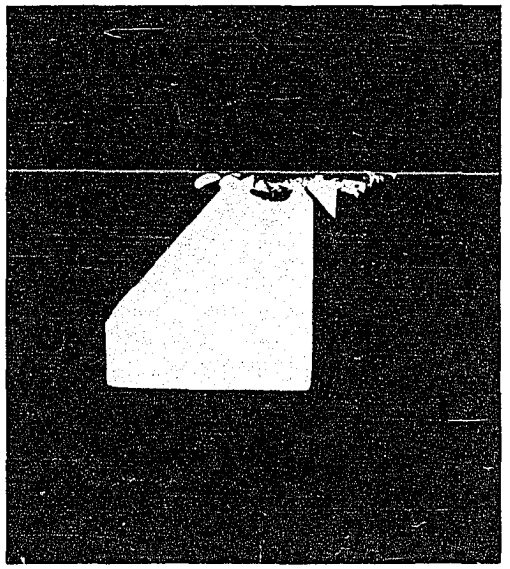

b

Figure 15. Photomicrographs of slip lines observed in high purity yttrium. (a) $\{10\bar{1}0\}\langle 1\bar{2}10\rangle$ slip lines visible on a $\{1\bar{2}10\}$ face. 1400X magnification. (b) $(01\bar{1}0)[2\bar{1}\bar{1}0]$ and $(0001)[2\bar{1}\bar{1}0]$ slip lines on the free face of plane strain compression sample. 400X magnification

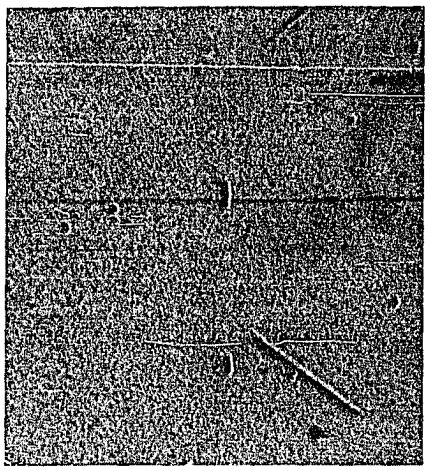

a

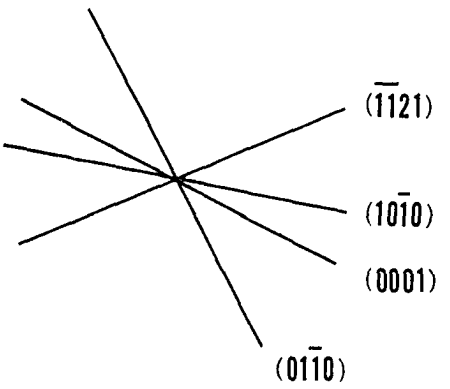

b

representative of what was generally observed. The straightness of the slip lines indicates little if any cross slip takes place between the basal and prism slip systems.

The two main twin modes in yttrium were easily distinguished from one another by their appearance. The $\{11\bar{2}1\}$ $\langle\bar{1}\bar{1}26\rangle$ twins were very narrow with straight parallel sides while the $\{10\bar{1}2\}\langle\bar{1}011\rangle$ twins were more the classic broad lenticular shaped twins. The purity of the material appears to have had a large effect on the width of the $\{11\bar{2}1\}\langle\bar{1}\bar{1}26\rangle$ twins with the width increasing from what looked like medium slip in commercial purity yttrium to medium width twins in high purity yttrium. These two main twins are shown in Figure 16.

The active slip modes in hcp metals have been analyzed by applying anisotropic elasticity theory to predict the elastic energy and ease of glide of dislocations in the basal and prism slip systems (65,66). Yoo and Wei (67) applied the theory for the case of zinc, Tyson (39) applied it to thallium, and Roy (68) applied it to cadmium, magnesium, zirconium, yttrium, and beryllium. The analysis was based on Foreman's result (66) that the elastic energy per unit length of a dislocation is given by

$$E = \frac{Kb^2}{4\pi} \ln \frac{R}{r_c}$$

where K is a constant and is a function of the elastic

Figure 16. The common twins in high purity yttrium. (a) $\{11\bar{2}1\}\langle\bar{1}\bar{1}26\rangle$ twins as observed on a $\{10\bar{1}0\}$ face. 400X magnification. (b) $\{11\bar{2}1\}\langle\bar{1}\bar{1}26\rangle$ and $\{10\bar{1}2\}\langle\bar{1}011\rangle$ twins as observed on a $\{10\bar{1}0$ face. 400X magnification. The $\{11\bar{2}1\}\langle\bar{1}\bar{1}26\rangle$ twins are narrow and straight sided while the $\{10\bar{1}2\}\langle\bar{1}011\rangle$ twins are broad and lenticular shaped

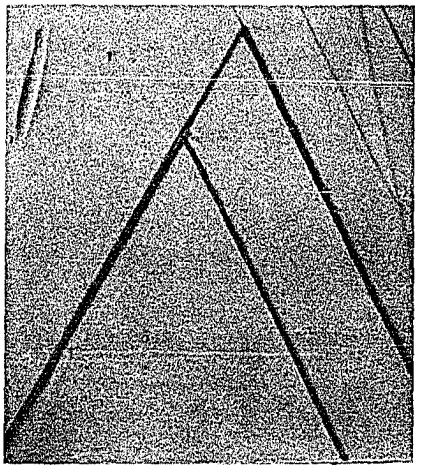

a

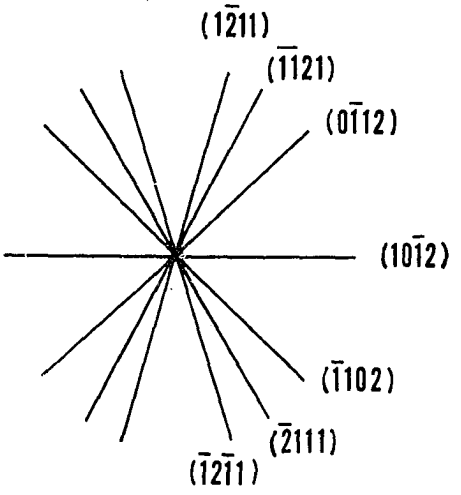
(1$\bar{2}$11)
($\bar{1}$121)
(01$\bar{1}$2)
(10$\bar{1}$2)
($\bar{1}$102)
($\bar{2}$111)
($\bar{1}$2$\bar{1}$1)

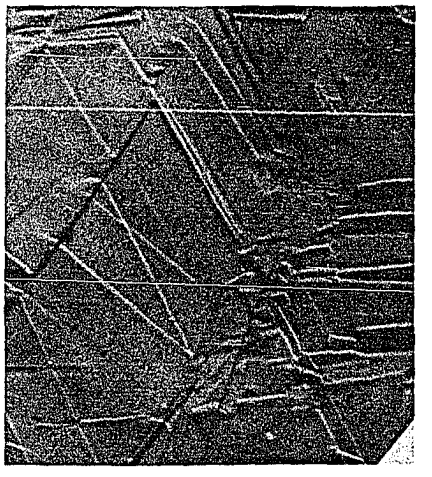

b

constants of the material and the orientation of both the Burgers vector and the tangent vector with respect to the crystal axes, R is the radius of the dislocation strain field, and r_c is the core radius. If the dislocation is oriented with respect to a set of three mutually perpendicular coordinates (X, Y, Z), with the tangent vector pointing in the +Z direction and the slip plane being the Y = 0 plane, a solution for K may be obtained. The solution is based on edge and screw dislocations of the above orientation having the property that they are parallel to a symmetry axis and perpendicular to a symmetry plane. Both edge and screw dislocations on the basal and prism planes have this property. Foreman's (66) solution for K was then

$$K_{edge} = (\bar{C}_{11}+C_{12}) \left| \frac{C_{66}\,(\bar{C}_{11}-C_{12})}{C_{22}\,(\bar{C}_{11}+C_{12}+2C_{66})} \right|^{\frac{1}{2}}$$

$$\bar{C}_{11} = (C_{11}C_{12})^{\frac{1}{2}}$$

where

$$K_{screw} = (C_{44}\,C_{55} - C_{45}^2)^{\frac{1}{2}} .$$

The C_{ij} of these equations are the transformed elastic constants which have been measured for the c-axis parallel to the Z axis and the a_1-axis parallel to the X axis. The transformation matrices are

$$\begin{vmatrix} 1 & 0 & 0 \\ 0 & 0 & 1 \\ 0 & -1 & 0 \end{vmatrix}$$

for basal glide and

$$\begin{vmatrix} 1 & 0 & 0 \\ 0 & 1 & 0 \\ 0 & 0 & 1 \end{vmatrix}$$

for prism glide.

Roy (68) discussed these results in terms of an ease of glide parameter, ξ/b, which is related to the dislocation width, and the elastic energy parameter, $Kb^2/4\pi$. The quantity ξ was defined as

$$= \tfrac{1}{2}KS_{66}d$$

where d is the interplanar spacing and S_{66} is an elastic compliance constant.

All of the authors found that the theory fitted the observed slip systems well for all cases considered except zirconium. It predicts yttrium should deform by basal glide if the basal stacking fault energy is low and by prism glide if the basal stacking fault energy is high. There have been no basal stacking fault energy measurements made on yttrium but the fact that slip occurs primarily on the prism system indicates a high stacking fault energy in the temperature range of this investigation according to the theory.

In summary, yttrium was shown to deform primarily by

$\{10\bar{1}0\}\langle 1\bar{2}10\rangle$ slip and $\{11\bar{2}1\}\langle \bar{1}\bar{1}26\rangle$ twinning. The secondary deformation modes are $(0001)\langle 11\bar{2}0\rangle$ slip and $\{10\bar{1}2\}\langle \bar{1}011\rangle$ twinning. C-axis compression samples fracture along the $\{11\bar{2}3\}$ plane after very little deformation. This lack of deformability and the existence of the fracture plane probably cause the fabricability problems inherent in yttrium.

B. Bicrystal Deformation and Grain Boundary Energy Studies

Yttrium was an ideal metal on which to test small angle boundary strengthening. Its limited number of slip systems simplified the analysis of the results, bicrystals of controlled orientation could easily be made, metal of good purity was available, and fairly reliable grain boundary energy measurements could be made due to its high solubility for the gaseous impurities carbon, nitrogen, oxygen, and hydrogen. This last property was important because the energy measurements were made from observations of thermal groove angles, a surface phenomena which can be affected by adsorbed gases or oxide layers.

1. Preparation and testing of bicrystal compression samples

The results of the deformation mode study showed that the primary slip system was the $\{10\bar{1}0\}\langle 1\bar{2}10\rangle$ system. With that in mind and wanting to keep as many potential variables constant as possible the following sample geometry was decided upon. The grain boundary was a $\{10\bar{1}0\}$ plane with the two component

crystals being stacked one on top of the other as in Figure 17b. This made the compression faces $\{10\bar{1}0\}$ planes and placed the grain boundary horizontal rather than vertical. Each component crystal was rotated one half the angle of misorientation, θ, in opposite directions about the compression axis. The samples were of square cross section with a height to width ratio of about 2:1. Typical dimensions were 0.475 x 0.475 x 0.950 cm. The two side faces were $\theta/2$ degrees from the (0001) and $\{1\bar{2}10\}$ planes. This particular geometry left the other two $\{10\bar{1}0\}$ planes equally inclined 30° from the compression axis in all cases. Furthermore, the $<11\bar{2}0>$ slip directions in these planes were also equally inclined 30° from the compression axis. This meant that there were two equally stressed slip systems in each component crystal of the bicrystal.

Each bicrystal was actually prepared (Figure 18) by sintering two single crystals together. Single crystal wafers approximately 0.475 cm thick were obtained by spark cutting along a $\{10\bar{1}0\}$ plane of one of the large yttrium crystals. Each wafer was then cut in half perpendicular to the $\{10\bar{1}0\}$ plane along a line $\theta/2$ away from the (0001) plane trace. Each half was then carefully hand lapped through 600 grit paper to remove the spark damaged layer and to expose a smooth flat surface. A bicrystal sandwich was then made by rotating one of the halves over onto the other, lightly clamped in a

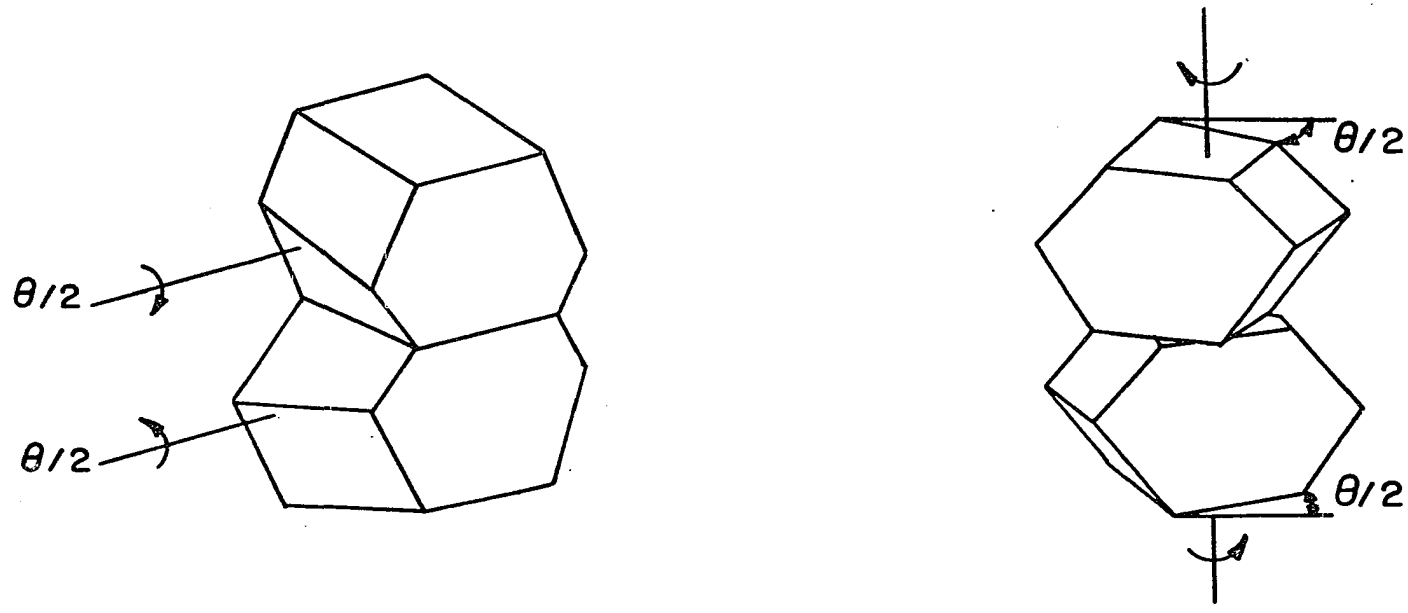

Figure 17. Models illustrating the relation of the component crystals of the bicrystals used in these experiments. (a) Tilt boundary model. (b) Twist boundary model. The load axis was perpendicular to the plane of the boundary in both cases

tantalum jig, and sintered together in a high vacuum furnace at 1673°K for twenty four hours. Once the sintering was completed the vertical faces were spark cut. The yield from this procedure was two bicrystals for each degree of twist orientation. Each pair of samples was hand lapped to remove the spark damaged layer on the newly cut faces, cleaned with alcohol, and reannealed at 1673°K for two hours, and cooled back to room temperature over a two hour period. They were then electropolished and the ends ground flat and parallel. Two X-ray Laue back reflection photographs were made for each bicrystal. The first showed the orientation of one of the component crystals as the bicrystal stood in its compression position. The second picture showed the orientation of one crystal with respect to the other. This was done by laying the sample on its $\{1\bar{2}10\}$ side and traversing the (0001) side from one compression end to the other with the X-ray beam. This superimposed the back reflection pattern from each component crystal on one photograph from which their relative orientations were measured.

The samples were then measured and compressed between oiled platens in the Instron machine at a cross head rate of 0.0127 cm/min. at room temperature. Twist misorientations from 0° to 10.9° were tested. A load-elongation curve monitored the deformation process with each test being interrupted as soon as yielding began. The yield load was determined by

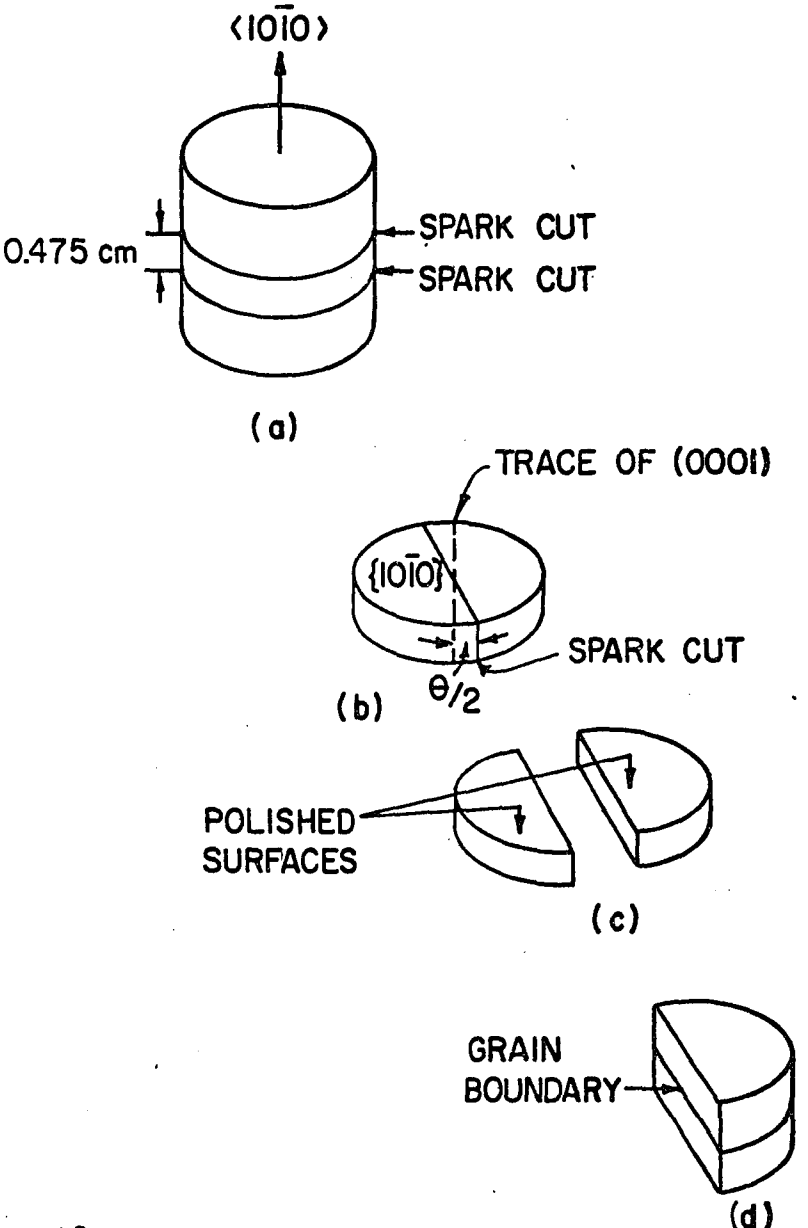

Figure 18. Steps in making bicrystal sandwich. (a) Single crystal wafer was spark cut from big crystal along a $\{10\bar{1}0\}$ plane. (b) Wafer was then rotated $\theta/2$ about the $\langle 10\bar{1}0\rangle$ direction and spark cut into two halves. (c) Corresponding faces of each half were polished flat and smooth. (d) The polished faces were placed in contact and sintered together

the point at which the load-elongation curve departed from a straight edge laid along the elastic portion of the curve. The critical resolved yield stress was calculated by assuming the area of the slip plane to be equal to the area of the slip plane of a single crystal of the same dimensions as the bicrystal whose orientation was that of either one of the component crystals of the bicrystal. The data was then plotted as critical resolved yield stress versus degree of twist.

A few tilt boundary samples were also made up and tested by the same procedure. They were tilted about a $\langle 11\bar{2}0 \rangle$ direction and covered the range of 0° tilt to 10.5° tilt.

2. Preparation and testing of relative grain boundary energy samples

One sample from each twist orientation was degreased after compression testing and annealed at $1673^{\circ}K$ for two hours to eliminate most of the effects of deformation. The only remaining effect was a slight amount of polyganization substructure. This was an acceptable state for measurement of the grain boundary energies.

The grain boundary energies were determined relative to the surface energy by a technique known as the thermal groove method (69,70). This is based on the fact that metal surfaces and grain boundaries have an energy associated with them. When a grain boundary intersects a surface, the grain boundary tries to minimize its energy by shrinking into the solid.

However this tends to pull the surface in the vicinity of the grain boundary into the material also. This has the effect of increasing the surface area and consequently the surface energy. The net result is a compromise which is a thermal groove. Figure 19 shows the profile of a thermal groove and the angles α_1 and α_2 which are measured experimentally when determining grain boundary energies by the thermal groove method. Thermal grooves can be seen without magnification so that large amounts of atoms must be rearranged when they form. This can only happen near the melting point so thermal groove experiments are run at high temperatures. One further requirement to insure the groove having an equilibrium profile is to provide sufficient metal atoms in the atmosphere surrounding the sample so that an equilibrium vapor pressure is attained. This is done by enclosing the sample in a container of the same material as the sample.

The equilibrium expression for the energy balance at a thermal groove is

$$\cos \bar{\alpha} = \cos \frac{(\alpha_1+\alpha_2)}{2} = \tfrac{1}{2}\gamma^g/\gamma^s$$

or

$$R_\gamma = \gamma^g/\gamma^s = 2\cos \bar{\alpha}$$

where γ^s is surface energy

γ^g is grain boundary energy

α_1 are the half groove angles at the root of the groove

$\bar{\alpha}$ is the average root half angle.

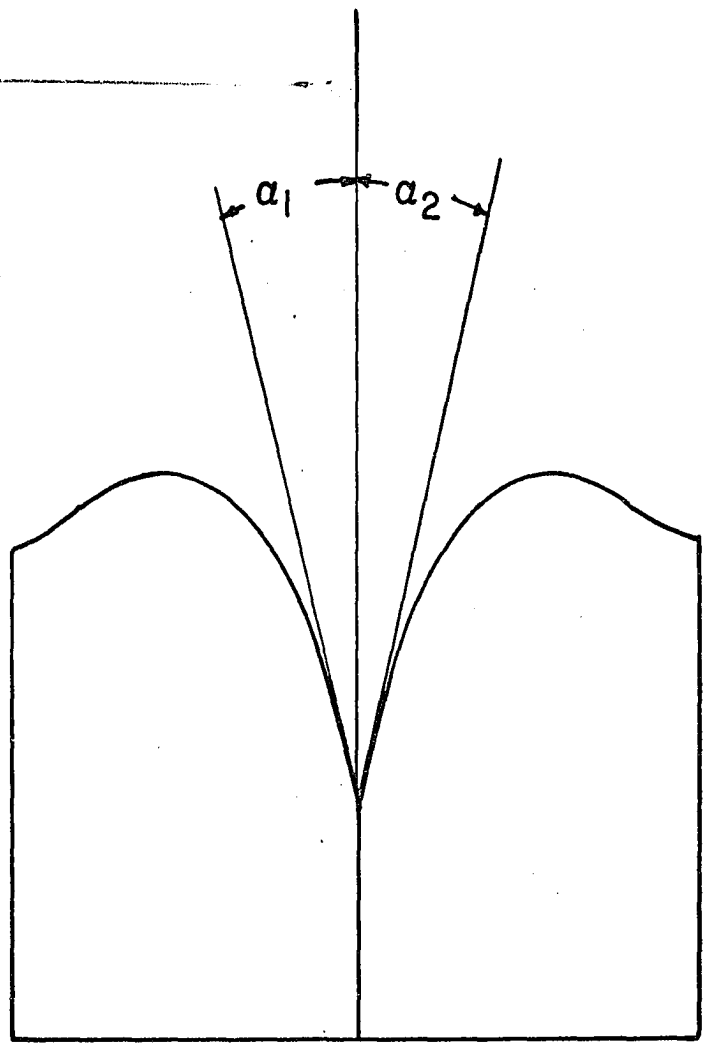

Figure 19. Model illustrating the shape of a thermal groove in a bicrystal. α_1 and α_2 are the root half angles of the groove

This expression shows that a measurement of the root half angle will give the grain boundary energy relative to the surface energy. If this is done as a function of the degree of twist, the variation of the energy ratio as a function of θ can be plotted.

The root half angle can be measured quite easily with an interference microscope. Gjostein (71) has given a complete analysis along with a discussion of the errors involved in this procedure. The interference microscope basically reveals changes in heights and interference bands can be thought of as contours of elevation. When an interference line meets a thermal groove, it dips along the sides of the groove until it hits the bottom and then rises up the other side until it meets the surface again. This is shown for one half of a hypothetical flat sided groove in Figure 20. From the diagram

$$\text{Tan}\,\kappa = \overline{CB}/\overline{OB}$$

$$\text{Tan}\,\alpha_1 = \overline{CB}/\overline{AB}$$

$$\frac{\text{Tan}\,\kappa}{\text{Tan}\,\alpha_1} = \overline{AB}/\overline{OB} = \sin\beta$$

Also, the interference condition for the reference plane being at a small angle, β, from the surface is

$$L = \frac{\lambda/2}{\sin\beta}$$

or

$$\sin\beta = \frac{\lambda/2}{L}$$

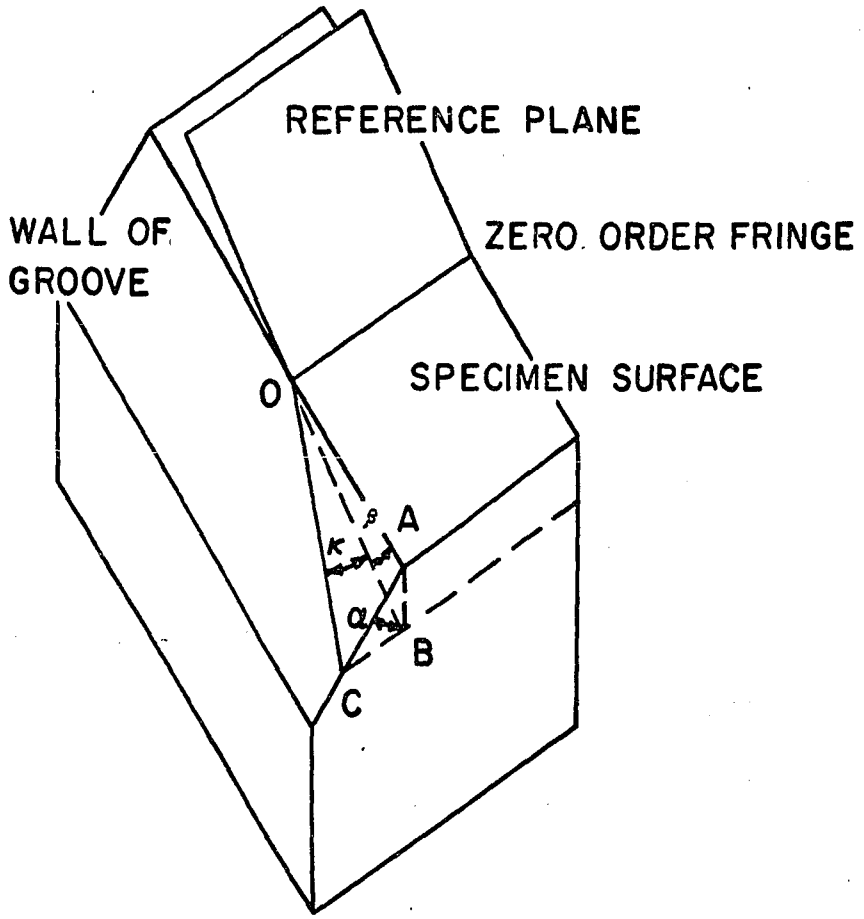

Figure 20. Model of one side of a hypothetical flat sided thermal groove illustrating how the interference fringe follows the contour of the surface

where L is the fringe spacing and λ is the wavelength of the light. The thermal groove relation follows by equating the two expressions for sin β and rearranging terms to get

$$\text{Tan } \alpha_1 = \frac{L}{\lambda/2} \text{ Tan } \kappa$$

The determination of $\bar{\alpha}$ is done by measuring α_1 and α_2 for the groove. This is done by keeping the fringe spacing small enough to enable a photomicrograph to be taken of a number of fringes intersecting the groove and averaging the α_i for each fringe. Figure 12a (page 49) shows an interference micrograph of a 5.5° twist thermal groove.

The actual experimental procedure was as follows. Each sample was polished through Linde B abrasive on a wax lap. This was found necessary in order to produce the extremely flat and smooth surface required by interference microscopy. The nominal $\{1\bar{2}10\}$ sides of the bicrystals were chosen because they seemed to produce the best shaped grooves. All the samples were placed in an yttrium foil lined tantalum pill box containing a thermocouple well in its center. A chromel-alumel thermocouple was placed in the well after the pill box was loaded in the high vacuum furnace. The samples were heated to $1523 \pm 5^\circ K$ for twenty-four hours and cooled rapidly to room temperature after the furnace power had been shut off. Each sample was then taken from the pill box and mounted on a glass slide. It was placed on the stage of a Zeiss interfer-

ence microscope and interference micrographs were taken by aligning the fringes perpendicular to the grain boundary. Fringe spacings on the order of 0.01 mm were used and magnified 810X so that from ten to fifteen measurements of the root half angles could be made on a given micrograph. The individual measurements were made by measuring α_1 and α_2 for each fringe with the aid of a mirror placed at the apex of the groove (Figure 21). The mirror was rotated about the apex until the side of the groove whose angle was being measured appeared to continue smoothly into the mirror. The complement of the acute angle between the mirror and the grain boundary was the half groove angle being measured. The results were plotted as 2 cos $\bar{\alpha}$ versus degree of twist. The average groove half angles, $\bar{\alpha}$, varied from 88° at 1° twist to 80° at 59.5° twist. Very low angle-of-twist grooves were quite shallow and the accuracy of the measurement of their groove half angles was definitely lower than for the higher angle of twist grooves. Also orientations of about a degree on either side of 7° and 12° twist had grooves whose bottoms were often filled with what was probably an oxide that formed on cooling. The accuracy of the values for these root half angles was also probably lower than for the other high angle boundaries. The interference lines for these orientations were extrapolated to the apparent positions of the apexes. Gjostein (71) estimated his errors in groove angle measure-

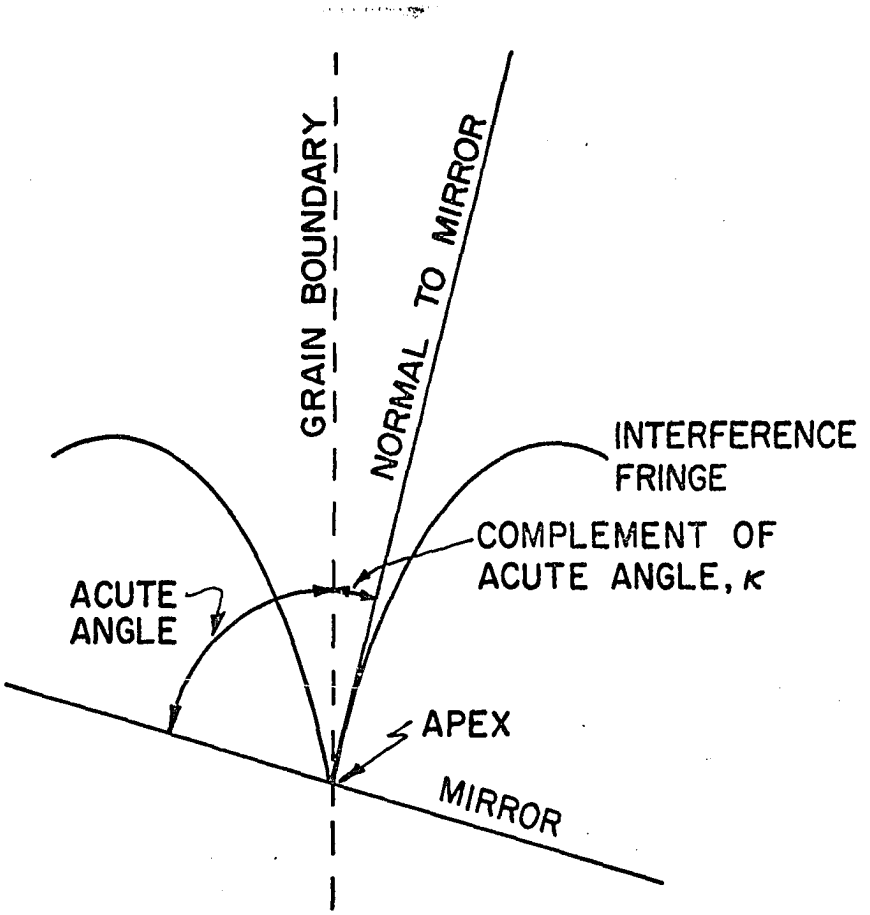

Figure 21. Diagram of the use of a mirror to aid in measuring the angle κ which is the root half angle of the interference fringe as it follows the contour of the thermal groove at a grain boundary

ments for copper to be on the order of ± 10%. The error here was probably ± 15%. It should be noted that the correction for the use of convergent illumination in the Zeiss interference microscope reported to be necessary by Tolmon and Wood (72) was incorporated in these results. It amounts to an increase of 10% in the fringe spacing.

3. Results of bicrystal compression experiments

The critical resolved yield stress for each bicrystal was plotted versus its degree of misorientation. The results are shown in Figure 22. The yield stress for both twist and tilt boundaries increased almost linearly to plateaus at about 5^{o} misorientation. The strength remained constant thereafter. The tilt boundaries appear to have been the more potent strengthener although the lack of sufficient data causes some uncertainty as to what the actual plateau value of the yield stress should be. These results will be discussed in terms of dislocation theory as soon as the model for the structure of the grain boundaries has been verified. This will be done by comparing the results of the thermal groove study with the Read-Shockley theory (56) and Gjostein and Rhines (57) study on [001] tilt and twist boundaries in copper.

4. Results and discussion of relative grain boundary energy experiments

The energies of the twist boundaries were determined

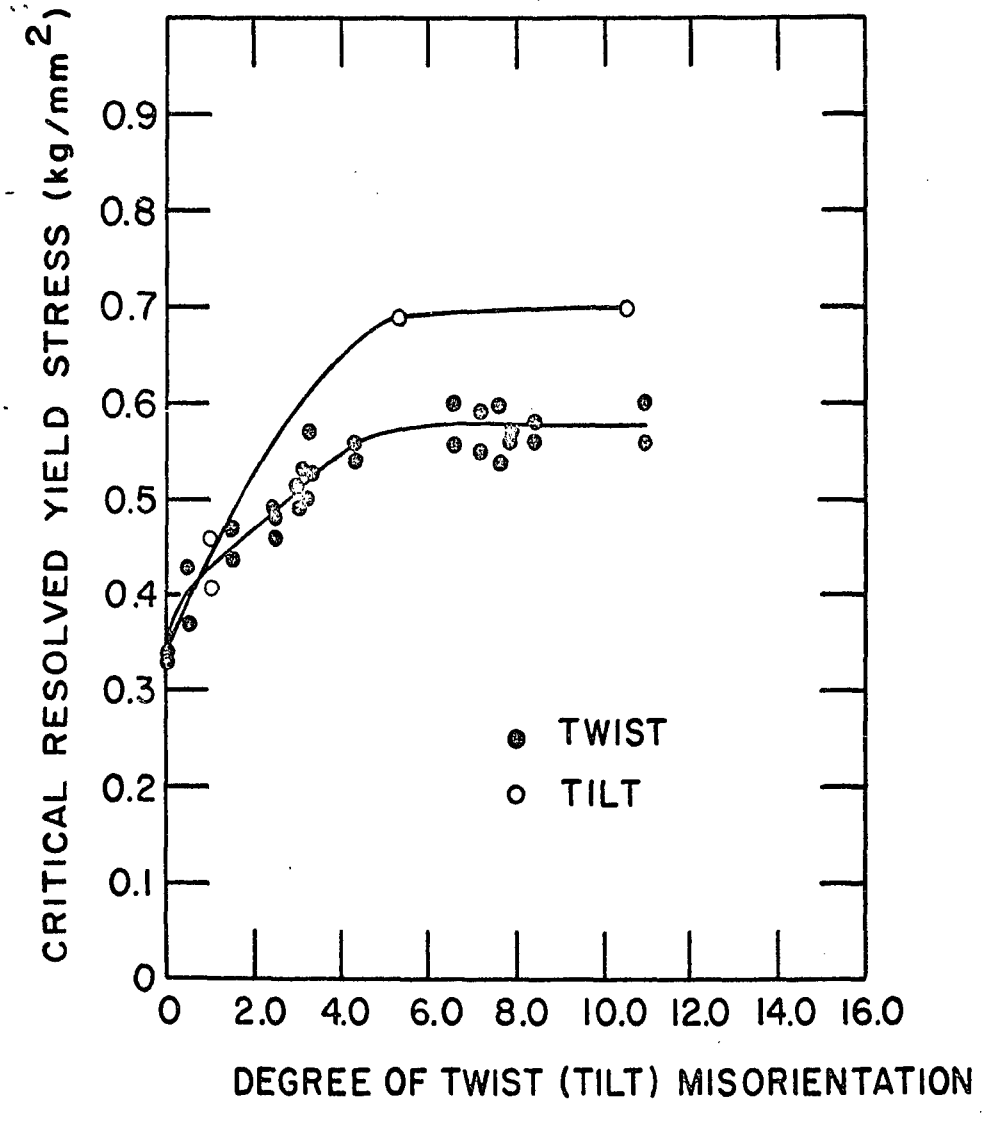

Figure 22. Plot of critical resolved yield stress versus θ for tilt and twist boundary samples

relative to the surface energy by the thermal groove technique discussed above. Figure 23 shows a plot of R_γ (equation 2, page 37) versus degree of twist and shows that the energy increases rapidly at first and then changes more slowly with an almost constant curvature as the degree of twist increases. Data were taken for degrees of twist up to 59.5° but values are plotted from 0° to 180° twist in keeping with the required symmetry of the effect. The curve is of the same general form and the relative grain boundary energies are of a similar magnitude as other observations made on grain boundary energy.

Gjostein and Rhines (57) verified the Read-Shockley grain boundary energy equation (equation 2, page 37) for small angle tilt boundaries in copper. Their plot of R/θ versus $\ln \theta$ changed shape in the region of about 4° tilt although they determined the parameters R_0 and A for the small angle region by a least squares plot which included data up to 12° tilt. Their value of R_0 in the small angle region was 0.91 and their value of A for that region was -0.72.

The results of this investigation are plotted in Figure 24. It can be seen that the data here fall on two lines of different slope too but the transition comes at about 8° instead of 4°. The values of R_0 and A for the small angle region are 1.28 and -0.98. If the Read-Shockley theory is correct, then these values for R_0 and A should yield reason-

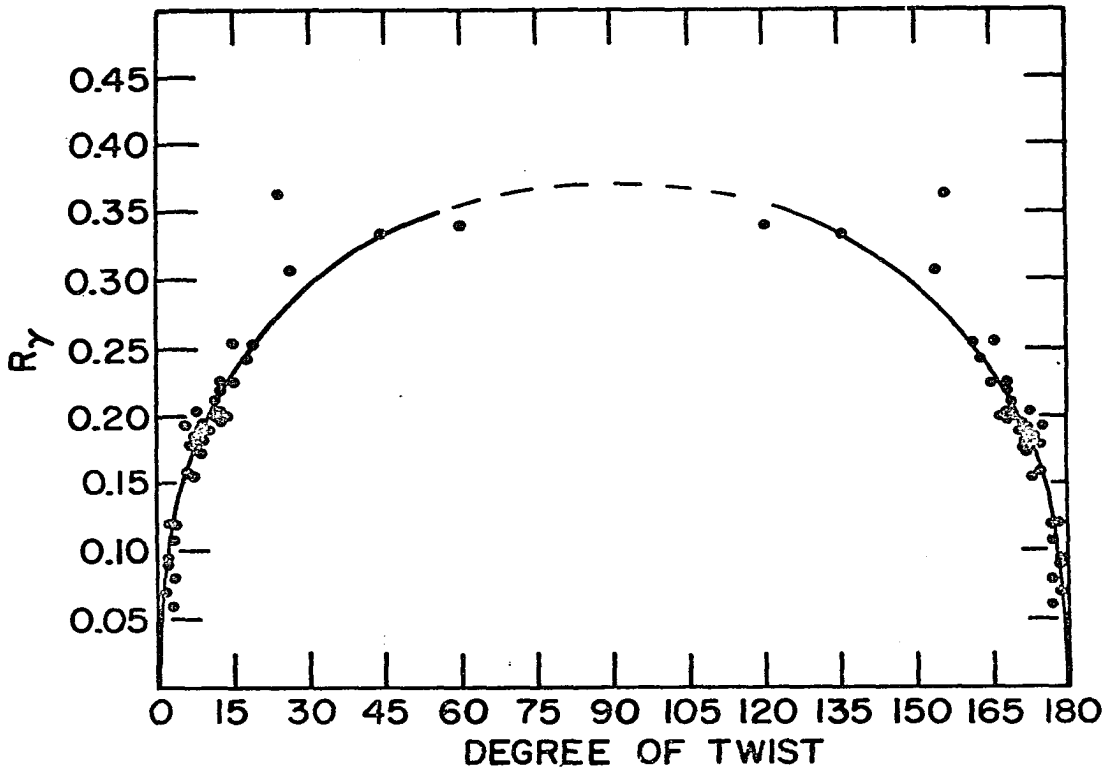

Figure 23. Plot of R_γ versus degree of twist for yttrium at 1523°K

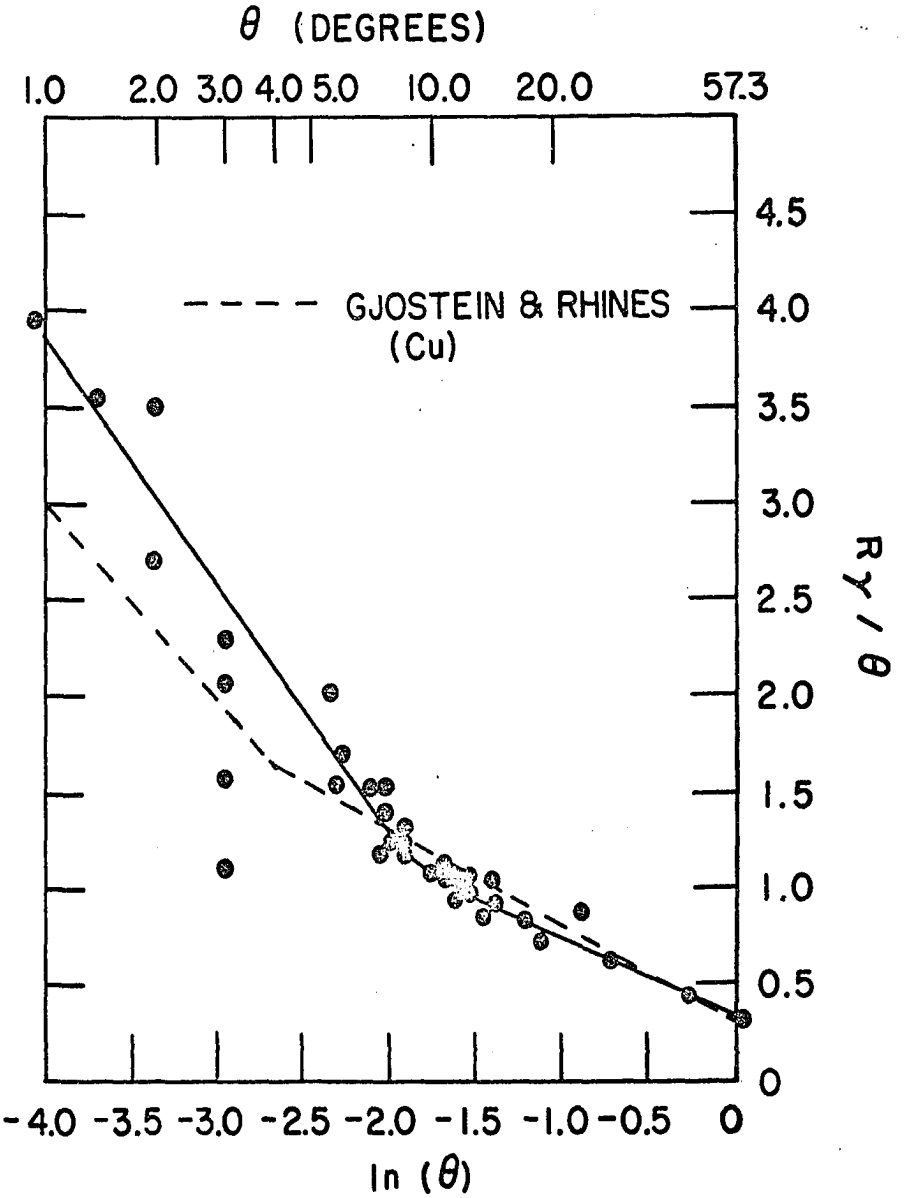

Figure 24. Plot of R_γ/θ versus ln θ for $[10\bar{1}0]$ twist boundaries in yttrium and [001] tilt boundaries in copper

able results in the expressions that contain them.

One calculation that makes use of R_o is that for determining the average surface energy, γ^s.

$$\gamma^s = E_o/R_o = \frac{\mu b}{2\pi R_o}$$

for a twist boundary containing two sets of screw dislocations of the same Burgers vector. For $\{10\bar{1}0\}$ twist boundaries in yttrium, b must be replaced by

$$\bar{b} = (b_1+b_2)/2.$$

Then

$$\gamma^s = \frac{\mu \bar{b}}{2\pi R_o} = 1460 \text{ erg/cm}^2.$$

This is a very reasonable number for the surface energy and compares with 1670 erg/cm^2 for copper (71), 1400 erg/cm^2 for gold (73) and 1140 erg/cm^2 for silver (74).

Another useful comparison is the calculation for the average core energy of a screw dislocation

$$E_c = \frac{\mu \bar{b}^2 A}{2\pi} = 9.1\text{x}10^{-6} \text{ erg/cm}$$

This compares with the approximate value of

$$E_c \approx \frac{\mu \bar{b}^2}{10} = 7\text{x}10^{-6} \text{ erg/cm}$$

according to Weertman and Weertman (75). So it appears that the theoretical values calculated for the surface energy and the screw dislocation core energy based on thermal groove

data from these experiments agrees with the expected values for these quantities very well.

The large difference in the transition point from low to high angle behavior between copper (4^{o}) and yttrium (8^{o}) is disconcerting if both are to obey the Read-Shockley theory. However if the dislocation structure of the tilt boundaries of Gjostein and Rhines (57) is considered the discrepancy is reduced considerably. They postulated the [001] tilt boundary in copper to be composed of an array of two types of parallel edge dislocations whose tangent vectors were parallel to the [001] direction. The first type had a $\sqrt{2}/2$ b [110] Burgers vector and the second type had a $\sqrt{2}/2$ b $[1\bar{1}0]$ burgers vector. The resultant tilt component contributed by each dislocation was then 0.707b. Therefore for a given amount of tilt the spacing in this boundary was 0.707 times that for a simple tilt or twist boundary. Furthermore, samples in the 0.6^{o} to 6.0^{o} tilt range contained asymmetric tilt boundaries. This means that the plane of the grain boundary was not parallel to the [001] direction. Weertman and Weertman (75) show that an asymmetric boundary such as this requires another set of edge dislocations such as this requires another set of edge dislocations with a third Burgers vector to be added to the array. This further complexity could have caused the effective dislocation spacing to become even smaller for a given tilt. The net result is that core overlap is to be expected

to begin considerably earlier for these samples than for the case of yttrium. This is again in agreement with the observations.

Therefore, the energies of the twist boundaries of this investigation appear to obey the Read-Shockley theory for low angle grain boundaries so that the dislocation models already described can be applied to them. This is based on the agreement with experiment of the values of the surface and screw dislocation core energies which were computed from the parameters derived from the thermal groove data. Also the shape and magnitude of the R/θ versus $\ln \theta$ curve for yttrium containing twist boundaries agreed with the same curve for copper containing tilt boundaries. Gjostein and Rhines (57) had previously verified the Read-Shockley equation for copper.

5. Discussion of small angle bicrystal strengthening results

Now that twist boundaries in yttrium have been shown to be composed of the classical small angle dislocation structure of two perpendicular arrays of parallel screw dislocations the strengthening effect can be discussed in terms of dislocation theory. Earlier it was shown that there are seven forces which arise due to the grain boundary in a bicrystal. The magnitude of these forces will now be discussed and the one most likely to have caused the strengthening will be determined. The seven forces once again are due to:

1. Incompatibility of strain across the grain boundary.

2. A change in the shear modulus from one component crystal to the other.
3. A change in the force law between the atoms in the extension of the slip plane of one crystal into the other.
4. The interaction of the stress field of the grain boundary with the stress field of the glide dislocation.
5. The formation of attractive junctions.
6. The formation of jogs in the glide and boundary dislocations as the glide dislocations pass through the boundary.
7. The dragging of jogged segments of the glide dislocation after it has passed through the boundary.

The first force will arise if the compatibility conditions are not met. A sample calculation for a θ^{o} twist boundary shows the general result for both twist and tilt boundaries in samples of the geometry used in these experiments. If each component crystal is rotated $\theta/2$ in opposite directions about the Z' axis with component crystal A being rotated clockwise and component crystal B being rotated counterclockwise, the strain compatibility equations at the grain boundary are

$$\epsilon'^{A}_{xx} = \epsilon'^{B}_{xx}$$

$$\epsilon'^{A}_{yy} = \epsilon'^{B}_{yy}$$

$$\epsilon'^{A}_{yx} = \epsilon'^{B}_{yx} .$$

Figure 5b (page 19) shows the coordinate systems for the samples used in these experiments and Figure 25 shows the rotations just described. The transformed strain components are

$$\epsilon'^{A}_{xx} = a^{A}_{xz}a^{A}_{xy}\epsilon^{A}_{zy} = m^{A}\epsilon^{A}_{zy}$$

$$\epsilon'^{A}_{yy} = a^{A}_{yz}a^{A}_{yy}\epsilon^{A}_{zy} = n^{A}\epsilon^{A}_{zy}$$

$$\epsilon'^{A}_{yx} = \tfrac{1}{2}[a^{A}_{yz}a^{A}_{xy}+a^{A}_{xz}a^{A}_{yy}]\epsilon^{A}_{zy} = p^{A}\epsilon^{A}_{zy}$$

and

$$\epsilon'^{B}_{xx} = a^{B}_{xz}a^{B}_{xy}\epsilon^{B}_{zy} = m^{B}\epsilon^{B}_{zy}$$

$$\epsilon'^{B}_{yy} = a^{B}_{yz}a^{B}_{yy}\epsilon^{B}_{zy} = n^{B}\epsilon^{B}_{zy}$$

$$\epsilon'^{B}_{yx} = \tfrac{1}{2}[a^{B}_{yz}a^{B}_{xy}+a^{B}_{xz}a^{B}_{yy}]\epsilon^{B}_{zy} = p^{B}\epsilon^{B}_{zy}$$

and the direction cosines, a_{ij}, are

Slip system 1		Slip system 2	
$a^{A}_{xz} = +a$	$a^{B}_{xz} = +a$	$a^{A}_{xz} = +a$	$a^{B}_{xz} = +a$
$a^{A}_{xy} = -b$	$a^{B}_{xy} = -b$	$a^{A}_{xy} = +b$	$a^{B}_{xy} = +b$
$a^{A}_{yz} = -c$	$a^{B}_{yz} = +c$	$a^{A}_{yz} = -c$	$a^{B}_{yz} = +c$
$a^{A}_{yy} = +c$	$a^{B}_{yy} = -c$	$a^{A}_{yy} = -c$	$a^{B}_{yy} = +c$

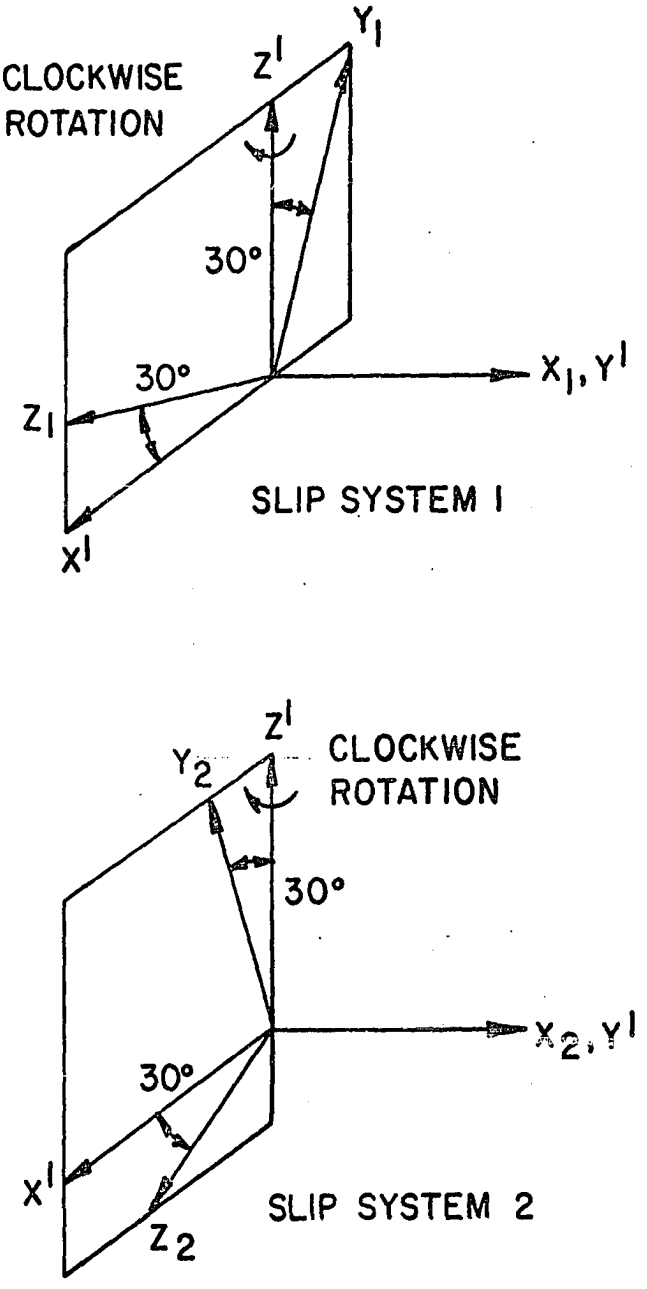

Figure 25. Relation of the XYZ coordinates to the X'Y'Z' coordinates for the two slip systems in $[10\bar{1}0]$ twist boundaries in yttrium

where a, b, and c are the values of the a_{ij} for any given θ. In checking for compatibility it is found that

Slip system 1	Slip system 2
$m^A = -ab = m^B$	$m^A = +ab = m^B$
$n^A = -c^2 = n^B$	$n^A = +c^2 = n^B$
$p^A = \frac{1}{2}(ac+bc) = -p^B$	$p^A = \frac{1}{2}(-ac-bd) = -p^B$

Therefore for each slip system the normal strains were compatible while the shear strains were equal in magnitude but of opposite sign. Also the magnitudes were the same for each type of strain in both slip systems so that if both operated simultaneously a shear strain of one could have become compatible with the corresponding shear strain of the other and vice versa thus making the whole bicrystal compatible. Both slip systems could have operated simultaneously to start with at least since they both initially had the same resolved shear stress on them. Therefore macroscopic compatibility was met for yielding and no stress should have arisen to strengthen the bicrystals due to this source.

It should be noted in support of the above discussion that Davis et al. (16) have shown experimentally that for aluminum containing a 45° misorientation grain boundary and two or more equally favored slip planes no change in the stress-strain curve over single crystals was observed.

The second force, that due to a change in shear modulus from one crystal to the other should have been nonexistent for three reasons. The first is that Smith and Gjevre (76) determined the elastic constants for yttrium and have shown that it has quite low anisotropy. The second is that the symmetry due to rotation of each component crystal in opposite directions would not allow the modulus to change in going from one crystal to the other. The third reason is that the small misorientation angles used in these experiments precluded any large change in the modulus. Thus this force is ruled out as a strengthener for the samples used in this study.

The third force which is due to the change in the force law between the atoms in the extension of the slip plane of one crystal into the other could cause strengthening of non dislocation boundaries but not dislocation boundaries. This is because the strain field of a glide dislocation will be smoothly transferred onto the slip plane in the other crystal by the dislocations in the grain boundary. However, once the misorientation becomes so great that core overlap occurs in the boundary it ceases to be composed of discreet dislocations and the strain field of the glide dislocations cannot then be transferred to the slip plane in the second crystal. It is for this case that this force can come to be the dominent strengthener. It is a short range force and will be of the order of $\mu/30$ at a distance of 1b from the boundary. The

strengthening for these samples occurred in the small angle region and had become constant by the time the dislocation model ceased to be correct. Therefore this force should not have been the cause of the observed strengthening.

The fourth through sixth forces are all concerned with glide dislocations interacting with the grain boundary dislocations. One would initially think that both edge and screw glide dislocations would have to be considered when dealing with these forces but only the edge dislocation case had to be considered for these samples. This is because a screw dislocation would have one end anchored in the grain boundary and the other end free with the result being that the free end would rotate around to an edge position as in Figure 26. Therefore only the edge case has to be considered.

The geometry of the situation is shown by Figure 27a and Figure 28a. The edge dislocation is perpendicular to one set of boundary screw dislocations and parallel to the other set. Its slip plane intersects the boundary at an angle of 60^{o}. The Burgers vector of the array of dislocations parallel to the glide dislocations is of the C[0001] type and the Burgers vector of the array of dislocations perpendicular to the glide dislocations is of the $a/3\langle 11\bar{2}0\rangle$ type. Both types are legitimate perfect dislocations according to Frank and Nicholas (77).

The fourth force arises due to the interaction of the

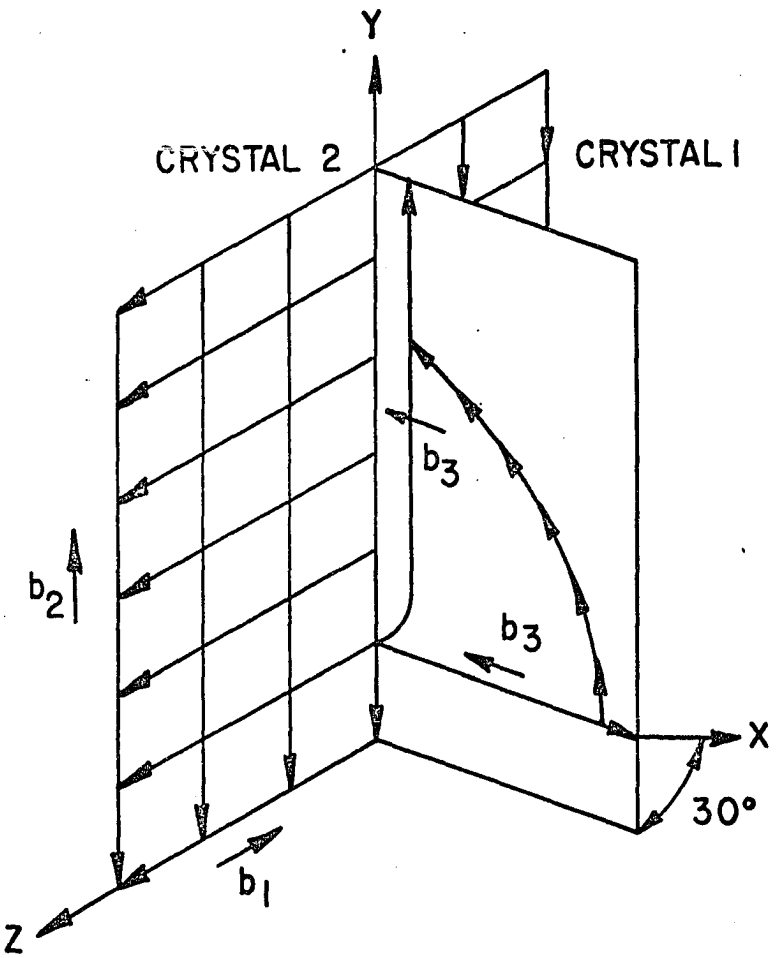

Figure 26. Model illustrating screw dislocation rotating to edge configuration because of the $[10\bar{1}0]$ twist boundary in yttrium

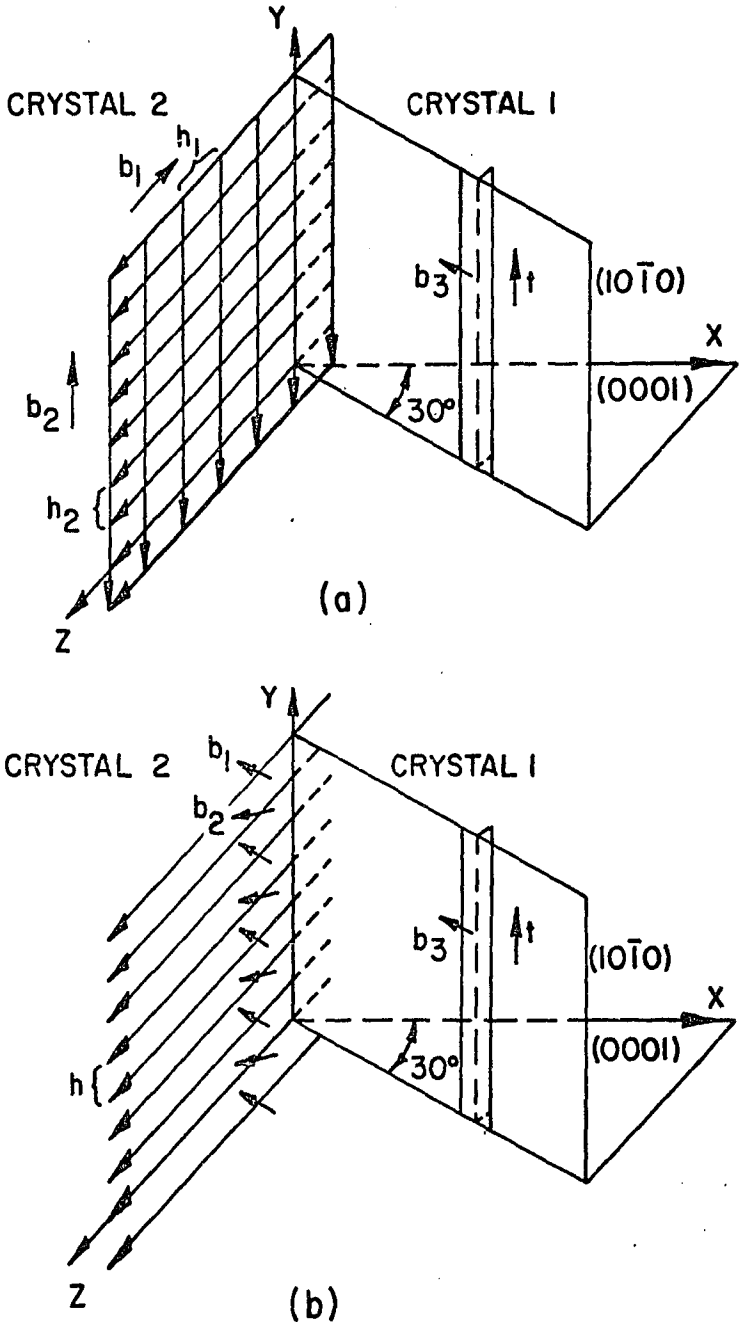

Figure 27. Geometry of grain boundaries and glide dislocations before intersection
(a) Edge dislocation approaching $[10\bar{1}0]$ twist boundary
(b) Edge dislocation approaching $[11\bar{2}0]$ tilt boundary

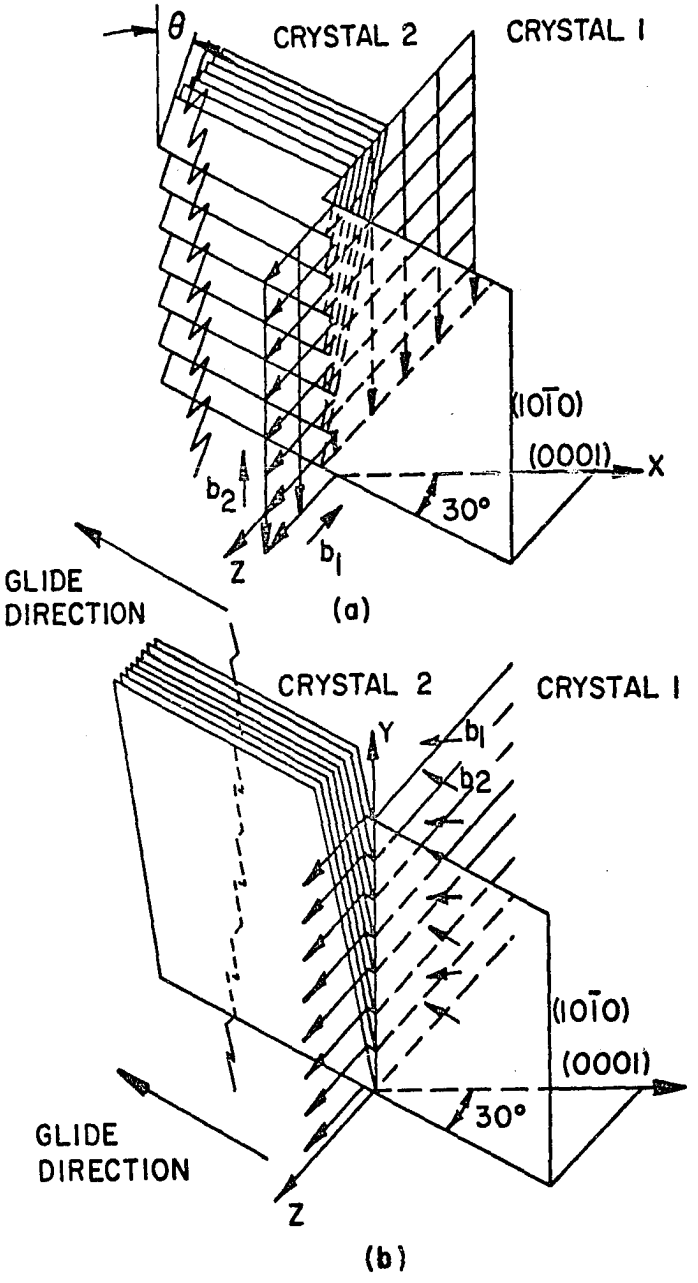

Figure 28. Geometry of grain boundaries and glide dislocations after intersection
(a) Edge dislocation after penetrating $[10\bar{1}0]$ twist boundary
(b) Edge dislocation after penetrating $[11\bar{2}0]$ tilt boundary

the stress field of the grain boundary with the stress fields of the glide dislocations. This requires knowledge of the stress field of the boundary which is calculated by aligning one array parallel to the Z axis and in the Y-Z plane. This puts the other array parallel to the Y axis and in the Y-Z plane. The stress field of the boundary is then a superposition of the stress fields of each of the two component arrays so that the interaction force between the boundary and the glide dislocations is the sum of the interaction forces between each component array and the glide dislocations. Weertman and Weertman (75) show that there is no interaction between parallel edge and screw dislocations so the problem reduces to determining the force between the glide dislocations and the array of screw dislocations perpendicular to them.

The force on the glide dislocation is determined by the Peach-Koehler equation which is (78)

$$F = \det \begin{vmatrix} i & j & k \\ t_x & t_y & t_z \\ G_x & G_y & G_z \end{vmatrix} ,$$

where i, j, and k are unit vectors parallel to the X, Y, and Z axes respectively and t_x, t_y, and t_z are components of the unit tangent vector of the dislocation. The expressions for the G_i are

$$G_x = \sigma_{xx}b_x + \sigma_{xy}b_y + \sigma_{xz}b_z$$

$$G_y = \sigma_{yx}b_x + \sigma_{yy}b_y + \sigma_{yz}b_z$$

$$\sigma_z = \sigma_{zx}b_x + \sigma_{zy}b_y + \sigma_{zz}b_z$$

where the σ_{ij} are the components of the stress field acting on the dislocation and the b_x, b_y, and b_z are components of the Burgers vector of the dislocation. The force due to the stress field of the array of screw dislocations in the grain boundary perpendicular to the glide dislocations is

$$F = \det \begin{vmatrix} i & j & k \\ 0 & 1 & 0 \\ G_x & G_y & G_z \end{vmatrix} = G_z i - G_x k$$

where

$$G_x = \sigma^a_{xz} b_z = -\ 1/2\ \sigma^a_{xz} b$$

$$G_z = \sigma^a_{zx} b_x = -\ \sqrt{3}/2\ \sigma^a_{xz} b$$

since $t = [010]t$ and $b = [-\sqrt{3}/2\ 0\ -1/2]b$ for this geometry. Therefore

$$F = F_x - F_z = -\ \frac{\sqrt{3}}{2}\ \sigma^a_{xz} b\ i + \frac{1}{2}\ \sigma^a_{xz} b\ k\ .$$

Resolving the forces onto the slip plane gives

$$F_1^{s.p.} \text{ due to } F_x = \frac{\sqrt{3}}{2}\ F_x$$

$$F_2^{s.p.} \text{ due to } F_z = \frac{1}{2}\ F_2$$

$$F^{s.p.}_{tot} = F^{s.p.}_{1} + F^{s.p.}_{2} = -\frac{3}{4}\sigma^{a}_{xz}b + \frac{1}{4}\sigma^{a}_{xz}b = -\frac{1}{2}\sigma^{a}_{xz}b.$$

The stress component of the array, σ^{a}_{xz}, acting on the glide dislocation is calculated by summing each σ_{xz} for an infinite array of parallel screw dislocations of regular spacing, h.

$$\sigma^{a}_{xz} = (1-\nu)D \sum_{n=-\infty}^{\infty} \frac{y+nh}{x^2+(y+nh)^2} \qquad \text{where } n = 0,\pm1,\pm2\text{---}$$

$$\text{and } D = \frac{\mu b}{2\pi(1-\nu)}$$

Setting $y/h = p$ and $x/h = q$ gives

$$\sigma^{a}_{xz} = \frac{(1-\nu)D}{h} \sum_{n=-\infty}^{\infty} \frac{p+n}{q^2+(p+n)^2}$$

$$= \frac{(1-\nu)D\pi}{h}\left[\cot(p+iq)\pi + \cot(p-iq)\pi\right]$$

or

$$\sigma^{a}_{xz} = \frac{(1-\nu)D\pi}{2h} \frac{\sin(2\pi y/h)}{\sinh^2(\pi x/h) + \sin^2(\pi y/h)} .$$

Therefore

$$F^{s.p.}_{tot} = -\frac{\mu b^2}{8h} \frac{\sin(2\pi y/h)}{\sinh^2(\pi x/h) + \sin^2(\pi y/h)}$$

when $y = nh/2$, $\qquad F^{s.p.}_{tot} = 0$

$y = (4n+1)h/4$, $\qquad F^{s.p.}_{tot} = F_{min} = -\frac{\mu b^2}{8h} \frac{1}{\sinh^2(\pi x/h) + \frac{1}{2}}$

$y = (4n+3)h/4$, $\qquad F^{s.p.}_{tot} = F_{max} = F_{min}$.

Plots of this force versus distance, X, are shown in Figure 29. Therefore the attractive and repulsive forces are equal in sign and alternate every h/2. This makes the total force on the dislocation zero so that the interaction between the stress fields of the boundary and the glide dislocations will not strengthen the bicrystal.

The fifth force is due to the formation of attractive junctions. This would appear to be a good possibility since the alternating repulsions and attractions acting on the glide dislocations would tend to warp them from straight lines to wavy lines. However a number of factors tend to negate this argument. The first is that the force is so short range that when it begins to become large enough to be significant the dislocation cores are already beginning to overlap and the validity of the force expression is in doubt. The second reason is that for the dislocation spacings (equation 1, page 33) present in these boundaries (57b to 11b) it is unlikely that the glide dislocations would warp enough to be strongly attracted or repelled by the boundary dislocations. Furthermore, even if the glide dislocations did warp considerably all that would happen is that they would pick up screw components nominally parallel to the X axis. The force arising from their interactions with the boundary screws would be nominally parallel to the boundary in the Y direction and this would not effect any repulsion or attraction on the glide

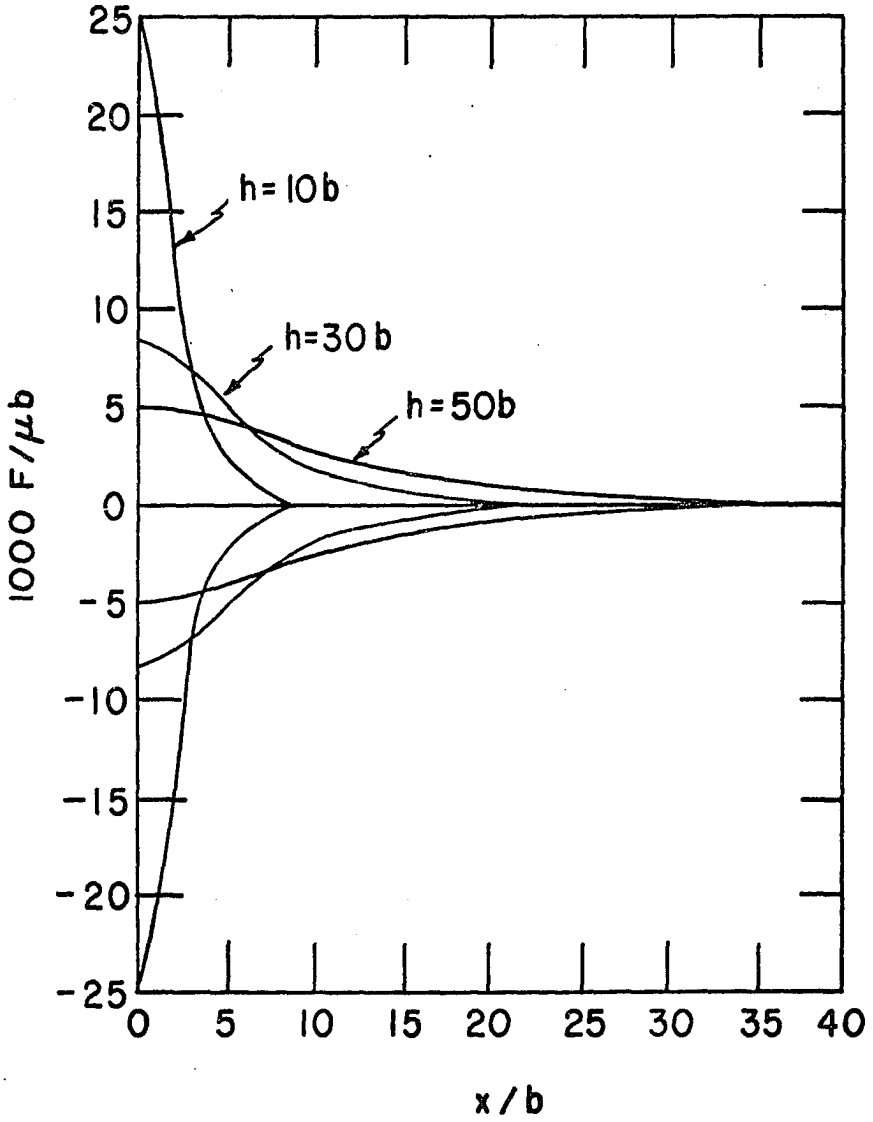

Figure 29. Plots of the maximum and minimum forces operating against an edge dislocation as it approaches $[10\bar{1}0]$ twist boundaries in yttrium

dislocations. Lastly, there are no other burgers vectors that could be formed from the burgers vectors of the glide and boundary dislocation burgers vectors which would be of lower energy. This eliminates the possibility of short lengths of glide and boundary dislocations joining together to form a segment of dislocation of different burgers vector which would require an increased glide force to dissociate again.

The sixth force, due to the formation of jogs in the glide dislocations and boundary dislocations, arises when the glide dislocations actually cut through the grain boundary. At each cutting point the glide dislocations pick up a 1b long jog due to their displacements by the boundary dislocations. The boundary dislocations in turn are jogged 1b due to their displacement by the glide dislocation. This process can be considered to be a short range interaction taking place over a distance of 1-10b depending on the deformation temperature (79-81). Therefore the force per intersection is just twice the energy to form jogs divided by the distance the force acts, 1-10b. It can be seen that the total force necessary to push a given length of dislocation through the grain boundary will vary as the dislocation density. This means that the force will increase as the angle of twist increases which is in qualitative agreement with the observed results.

The seventh and last force arises due to the necessity

of moving the jogged segments of the glide dislocations along the (0001) glide plane. This obviously required a larger force per unit length than for glide on the $\{10\bar{1}0\}$ plane because it is not the observed primary glide plane. Also, in these experiments, the (0001) plane was parallel to the stress axis so that no stress was resolved on it. Here as in jog formation the force to move the jogged dislocations should increase as the dislocation density of the boundary increases which is in qualitative agreement with the observed results.

In summary the seven forces which can arise due to the grain boundary in a bicrystal have been discussed qualitatively in relation to the experiments performed in this investigation. Only two, the force required to form jogs and the force required to drag jogs, were seen to be significant as potential causes of the observed strengthening. These two forces will now be examined quantitatively to determine which of them was the dominant strengthener. Jog dragging will be considered first and a 5° twist boundary will be used as an example for the calculations. The dislocation spacing of a 5° boundary is

$$h = \frac{57.3b}{5} = 11.5b.$$

This means that jogs 1b long would exist every 11.5b along the glide dislocations after they had intersected the grain boundary. It was determined from the plane strain experiment that the yield stress for slip on the $(0001)\langle 11\bar{2}0\rangle$ system is

about four times greater than the yield stress on the $\{10\bar{1}0\}$ $<\bar{1}2\bar{1}0>$ system so that the force to move the jog would be, at most, the same as the force to move a 4b extra length of dislocation every 11.5b of slip dislocation on the $\{10\bar{1}0\}$ plane. This results in a strengthening increment of 4b/11.5b times the yield force for slip on the $\{10\bar{1}0\}<\bar{1}2\bar{1}0>$ system or

$$\Delta F_{jog} = 0.5 \text{ dyne/cm.}$$

This compares with an observed strength increase of 0.8 dyne/cm. Therefore, this force which is about one half of the observed strengthening effect cannot, by itself, account for it. When the experimental value, obtained at room temperature, is corrected for thermal assistance, the discrepancy is even larger.

The force due to the formation of jogs was calculated by assuming the dislocation array of the boundary to be superposed on the existing internal structure of the component crystals. The resulting strengthening increment, ΔF, was then directly attributable to the boundary only. Conrad (79) shows experimental evidence based on thermally activated deformation experiments that the energy to form jogs is of the order of 0.80×10^{-12} erg/jog pair. This is based on the activation energy for thermally activated cutting of forest dislocations in aluminum which has been determined to be the rate controlling mechanism for that metal. For a 5° twist boundary there will be two jogs formed per 11.5b of glide dislocation line.

The total energy change per cm of dislocation, ΔE, then is the jog pair formation energy times the jog density or

$$\Delta E = 1.91 \times 10^{-6} \text{ erg/cm.}$$

The energy barrier for these samples was considered to be triangular shaped (Figure 30) with the base being the activation distance, d*, and the height being a force, ΔF. This shape should be a reasonable approximation based on the data of Basinski (80) and the review by Conrad (81). An approximation of d* at room temperature was made by performing strain rate change tests on a 2.5° twist boundary sample. An approximate activation volume model of

$$v^* = bhd^*$$

was chosen where v^* is the activation volume

b is the burgers vector

h is the grain boundary dislocation spacing.

Another expression for v^* based on strain rate change experiments is, according to Conrad (81),

$$v^* = \frac{kT \ln \dot{\epsilon}_2/\dot{\epsilon}_1}{\Delta\sigma},$$

where k is Boltzmans constant

T is absolute temperature

$\dot{\epsilon}_1$ is strain rate

$\Delta\sigma$ is the change in resolved shear stress as the strain rate is changed.

Equating the two expressions and solving for d* gives

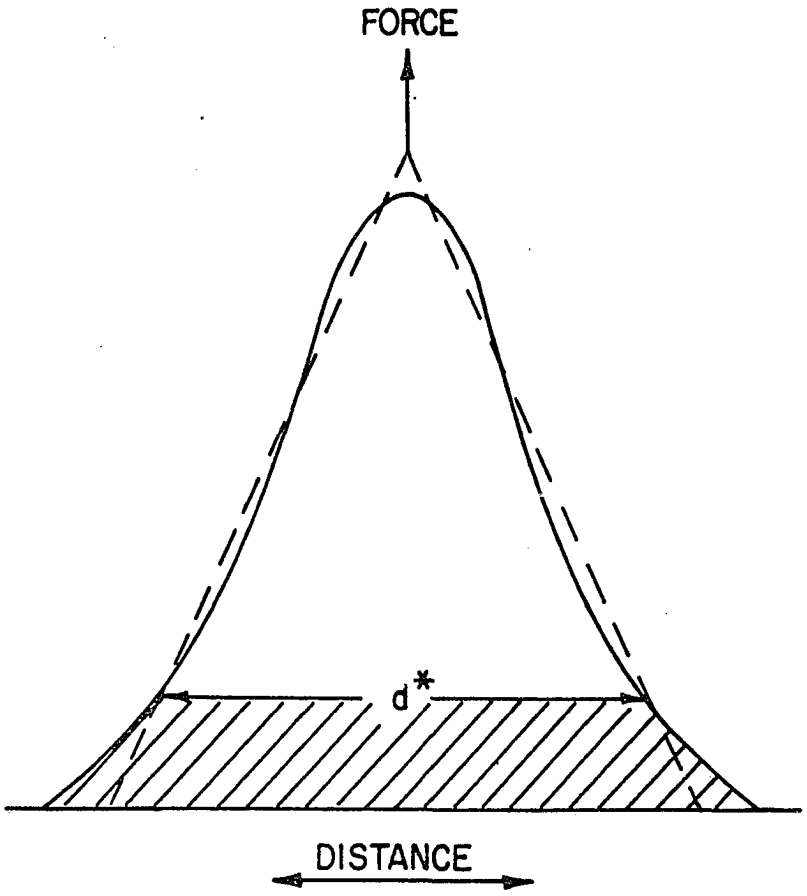

Figure 30. A force-distance curve and its triangular approximation. The total area under the curve is the energy to form a jog pair. The unhatched area represents energy provided by thermal assistance. The hatched area represents energy provided by the applied external stress. d* is the activation distance

$$d^* = \frac{kT \ln \dot{\epsilon}_2/\dot{\epsilon}_1}{bh\ \Delta\sigma} .$$

A 2.5° twist boundary sample was deformed at 298°K with a strain rate ratio of 10:1. The $\Delta\sigma$ resulting from this change was 0.052 Kg/mm^2 so that d* = 16b. This is a little large according to Basinski's (80) and Conrad's (79,81) values of 10b but is not unreasonable.

Using the value of d* = 16b, the force per cm of dislocation line is $\Delta F = 2\Delta E/16b = 6.6$ dyne. This is the value expected if no assistance were provided by thermal energy. The observed ΔF at 298°K was 0.8 dyne per cm of dislocation line. This is uncorrected for thermal assistance. The amount of thermal assistance was estimated by compressing two samples at 77°K and plotting a crude yield stress versus temperature curve. A single crystal sample and a 2.5° twist sample were compressed and the results are plotted in Figure 31. The curved shape of the plot was chosen because Koepke et al. (82) found polycrystalline yttrium obeys a logarithmic flow stress versus temperature curve. Extrapolation of the curve in Figure 31 to 0°K gives an estimated yield stress value of about five times the yield stress value for room temperature deformation. Therefore a ΔF of 4.0 dyne per cm of dislocation line results when correction for thermal assistance is added. This is excellent agreement with the theoretical value for ΔF of 6.6 dyne per cm of dislocation line.

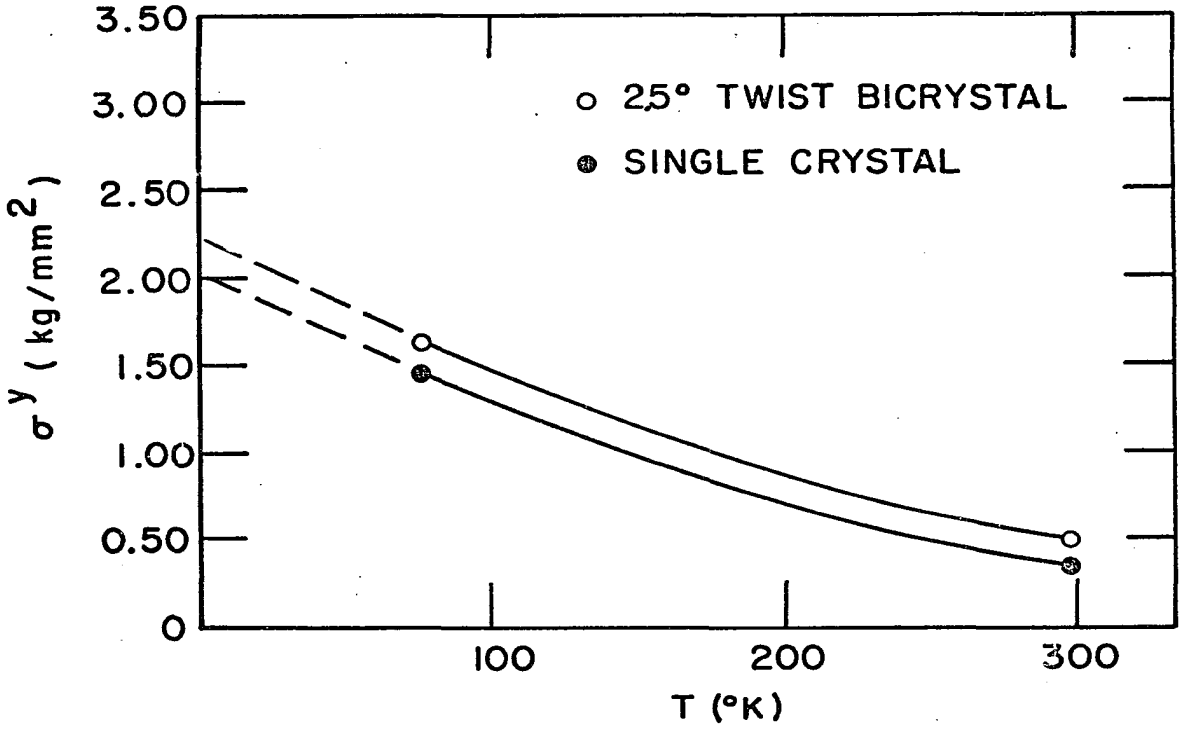

Figure 31. Critical resolved yield stress versus temperature in yttrium

The theoretical strengthening due to jog formation is shown in Figure 32 as a function of misorientation. The result based on the triangular shaped force-distance curve and thermally activated deformation is the only force in agreement with the observed strengthening so that jog formation appears to be the dominant strengthening mechanism for twist boundaries in yttrium. The increasing deviation with misorientation is probably due to the inability of the simple models used in the above discussion to hold for higher boundary dislocation densities.

It was decided to make a few tilt boundary samples in order to check the jog strengthening mechanism further. The samples had the same basic geometry as the twist boundary samples with the grain boundary being parallel to the compression faces and the vertical faces being the $\{1\bar{2}10\}$ plane and a plane $\theta/2$ from the (0001) plane. The tilt axis was the $\langle 11\bar{2}0\rangle$ direction parallel to the compression faces. Each half was rotated $\theta/2$ degrees in opposite directions about the tilt axis. All preparation and testing methods were exactly as for the twist boundary samples. The resulting yield stress versus degree of tilt curve while somewhat sketchy indicates the strengthening occurs at a more rapid rate and ultimately to a higher value than for the twist boundary curve. This is shown in Figure 20 (page 75).

The classic symmetrical tilt boundary is composed of an

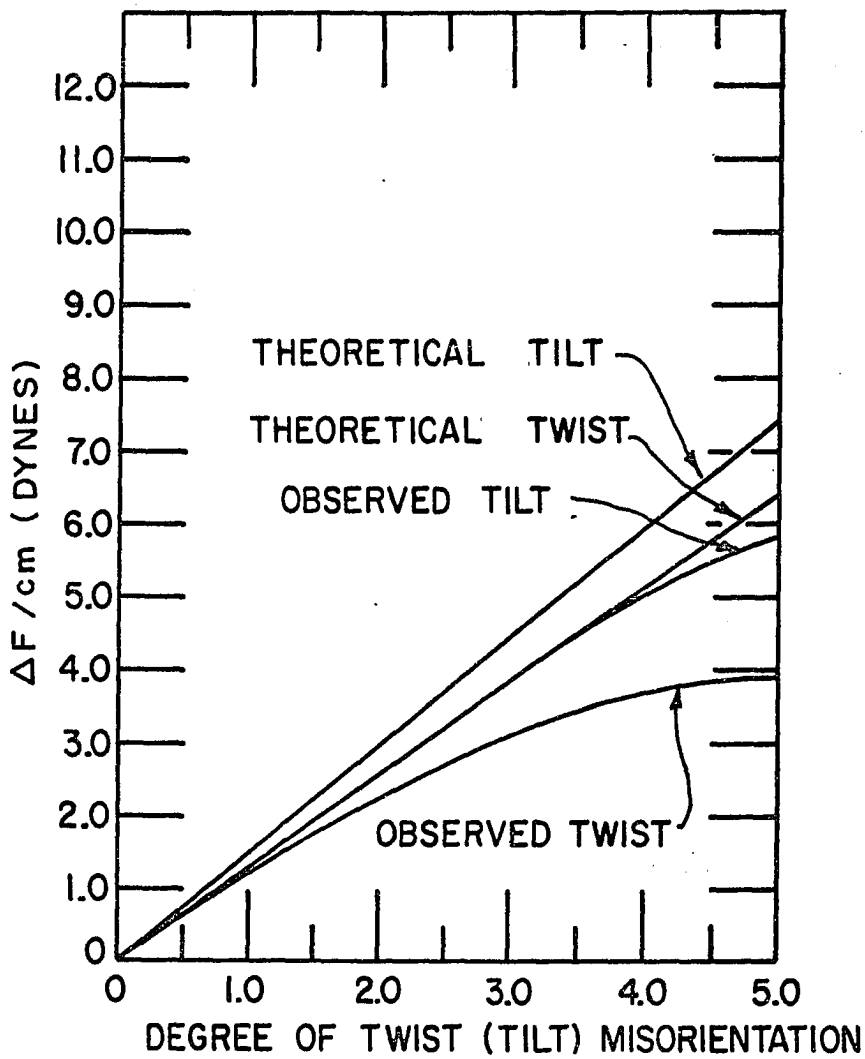

Figure 32. Theoretical and observed strengthening due to jog formation in small angle boundaries of yttrium. Plot is corrected to $0^{\circ}K$

array of parallel edge dislocations stacked one above the other and separated by a uniform distance, h, but it is impossible to do this with the particular tilt boundary used in these experiments. Instead, an array of mixed dislocations is envisioned to have been the correct model. The array consisted of two different types of mixed dislocations stacked alternately one above the other. The tangent vectors all were parallel and the screw components of each pair cancelled each other out so that the net effect was similar to the classical one. The Burgers vectors of each set were of the normal $\langle 11\bar{2}0 \rangle$ type but were rotated 30° in opposite directions from the normal to the plane of the boundary and were in the plane perpendicular to the boundary which intersected it along the lines of dislocations. Figure 25b (page 89) shows this orientation and a dislocation before its intersection with the boundary. Figure 26b (page 93) shows the jogged dislocation and boundary after intersection.

The forces due to incompatibility, change in shear modulus, and change in slip plane force law did not contribute any significant strengthening for the same reasons as for the screw case. Certainly jog formation should have been at least as potent a strengthener as for screws and the jog dragging force should have been of the same magnitude as for screws. This leaves the interaction with the stress field and attractive junctions forces to be considered.

The calculation of the stress field for the tilt boundary is similar to the calculation for the screw array. The tangent and Burgers vectors of the glide dislocations are

$$b = [-\frac{\sqrt{3}}{2} \quad 0 \quad -\frac{1}{2}]b$$

$$t = [\quad 0 \quad 1 \quad 0]t$$

$$F = \det \begin{vmatrix} i & j & k \\ 0 & 1 & 0 \\ G_x & G_y & G_z \end{vmatrix} = G_z i - G_x k$$

so that

$$F = -\frac{1}{2}\sigma_{zz} bi + \frac{\sqrt{3}}{2}\sigma_{xx} bk$$

Resolving forces onto the slip plane gives

$$F_{tot}^{s.p.} = 0.433b(\sigma_{xx}-\sigma_{zz})$$

This requires calculation of the stress components σ_{xx} and σ_{yy} for the array. For a single edge dislocation along the Z axis with b pointing in the negative X direction

$$\sigma_{xx} = Dy\frac{(3x^2+y^2)}{(x^2+y^2)^2} = 2x^2D\frac{y}{(x^2+y^2)^2} + D\frac{y}{x^2+y^2},$$

and

$$\sigma_{zz} = 2\ D\frac{y}{x^2+y^2}$$

The force due to the array then is

$$F_{tot}^{s.p.}\ \frac{0.433bD}{h}\left\{2q^2\sum_{n=-\infty}^{\infty}\frac{p+n}{[q^2+(p+n)^2]^2} + (1-2\nu)\sum_{n=-\infty}^{\infty}\frac{p+n}{q^2+(p+n)^2}\right\}$$

where $y/h = p$ and $x/h = q$ and $n = 0, \pm 1, \pm 2, \cdots$

Evaluation of the sums gives

$$\sum_{n=-\infty}^{\infty} \frac{p+n}{q^2+(p+n)^2\ 2} = \frac{-\pi^2}{4iq}\left[\csc^2(p+iq)\pi - \csc^2(p-iq)\pi\right]$$

$$= \frac{\pi^2}{4q}\ \frac{\sin(2\pi p)\ \sinh(2\pi q)}{\left[\sin^2(\pi p) + \sinh^2(\pi q)\right]^2}$$

and

$$\sum_{n=-\infty}^{\infty} \frac{p+n}{q^2+(p+n)^2} = \frac{\pi}{2}\left[\cot(p+iq)\pi + \cot(p-iq)\pi\right]$$

$$= \frac{\pi}{2}\left[\ \frac{\sin(2\pi p)}{\sin^2(\pi p) + \sinh^2(\pi q)}\ \right].$$

Therefore

$$F_{tot}^{s.p.} = \frac{0.433\pi bD}{2h}\left\{\frac{\pi x}{h}\ \frac{\sin(2\pi y/h)\sinh(2\pi x/h)}{\left[\sin^2(\pi y/h) + \sinh^2(\pi x/h)\right]^2}\right.$$

$$\left. + \frac{(1-2\nu)\ \sin(2\pi y/h)}{\sin^2(\pi y/h+\sinh^2(\pi x/h)}\right\}$$

when $y = nh/2$, $\qquad F_{tot}^{s.p.} = 0$

$y = (4n+1)h/4$,

$$F_{tot}^{s.p.} = F^{max} = \frac{0.866bD\pi}{h}\left\{\frac{2\pi x}{h}\ \frac{\left[\exp(2\pi x/h)-\exp(-2\pi x/h)\right]}{\left[\exp(4\pi x/h)+\exp(-4\pi x/h)+2\right]}\right.$$

$$\left. + \frac{(1-2\nu)}{\left[\exp(2\pi x/h)+\exp(-2\pi x/h)\right]}\right\}$$

$y = (4n+3)h/4$,

$$F^{s.p.}_{tot} = F^{min} = \frac{-0.866bD\pi}{h}\left\{\frac{2\pi x}{h}\,\frac{[\exp(2\pi x/h)-\exp(-2\pi x/h)]}{[\exp(4\pi x/h)+\exp(-4\pi x/h)+2]} + \frac{(1-2\nu)}{[\exp(2\pi x/h)+\exp(-2\pi x/h)}\right\}$$

$$F^{max} = F^{min}$$

The above analysis shows that just as for the screw dislocation boundary case the total force on the glide dislocation is zero but equal maximum and minimum forces occur every h/2 along the y axis. Plots for the maximum and minimum forces as a function of distance, X, from the grain boundary are shown in Figure 33. Thus as for the case of screw dislocations the forces due to the formation of attractive junctions or interactions with the stress field of the boundary have been ruled out as strengtheners.

It appears once again that the formation of jogs is the dominent strengthener. A sample calculation for a 5^{o} tilt boundary will show the general result. A 5^{o} tilt boundary will have a spacing of

$$h = (0.866)\frac{(51.3)}{(5.0)}b = 9.9b.$$

The total energy change per cm of dislocation, ΔE, is

$$\Delta E = 2.2\text{x}10^{-6} \text{ erg/cm.}$$

The energy barrier, ΔE, is again assumed to be triangular

shaped of base, 16b, so that

$$\Delta F = \frac{2\Delta E}{16b} = 7.5 \text{ dynes/cm.}$$

A plot of this strengthening versus degree of tilt is shown in Figure 28. The calculated strengthening is approximately 7 times greater than the observed uncorrected value of $\Delta F = 1.2$ dyne/cm for a 5^{o} tilt while the corrected value of 6.0 dyne/cm is in good agreement. Here, as for twist boundaries, thermal activation makes up most of the discrepancy and jog formation appears to be the dominent strengthening mechanism.

6. Discussion of large angle bicrystal strengthening results

The above discussion offers a reasonable explanation for the strengthening effect observed for the low angle twist and tilt boundaries which were studied in this investigation, It does not explain the stress plateaus or differences in the magnitudes of the plateaus between twist and tilt boundary samples.

An attempt will now be made to offer a qualitative explanation of the strength plateaus observed in the large angle bicrystal compression test results. One further bit of information, however, must be introduced. It has to do with the penetration of the boundaries by slip. After being compressed just past the yield point, two samples from the low angle boundary region where the strength increased with mis-

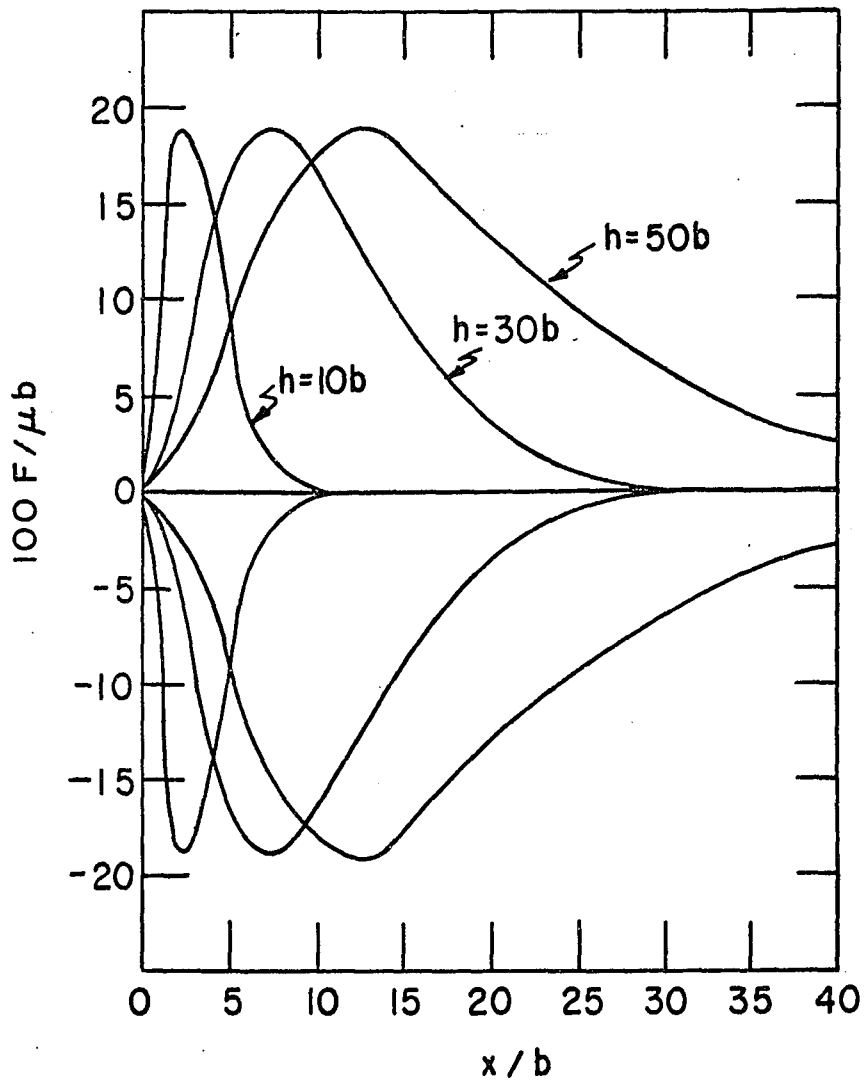

Figure 33. Plots of the maximum and minimum forces operating against an edge dislocation as it approached [11$\bar{2}$0] tilt boundaries in yttrium

orientation and two samples from the higher angle boundary region where the strength was constant had flats ground in them approximately parallel to the $\{11\bar{2}3\}$ plane. The flats were then electropolished and the samples recompressed enough to cause slip lines to become visible in the region of the grain boundaries. Photomicrographs of these samples are shown in Figure 34. The dislocations appear to have been able to easily penetrate the low angle boundaries but not the high angle boundaries since most of the slip lines were continuous across the low angle boundaries while most of the slip lines were stopped by the higher angle boundaries. This along with the stress plateaus indicates a change of strengthening mechanism from low to high angle behavior.

The new force must have been associated with the nucleation of dislocations on one side of the grain boundary by the combination of the external stress field and the stress field of single or piled up groups of dislocations on the other side of the boundaries since slip was shown in Figure 34 to be discontinuous across the grain boundaries. Also the fact that the plateau stress level was higher for tilt than twist boundaries indicates the geometry of the boundary had something to do with the nucleation stress. It is hard to visualize any of the seven forces discussed earlier as accounting for the different stress levels between the high angle tilt and twist boundaries. It appears that the edge dislocations

Fig. 34. Photomicrographs of slip lines intersecting the grain boundary in yttrium. The plane of each picture is the $\{11\bar{2}3\}$ plane. The grain boundary runs vertically in the center of each picture. All are 400X. (a) 1° twist boundary; (b) 8.5° twist boundary; (c) 1° tilt boundary; (d) 10.5° tilt boundary

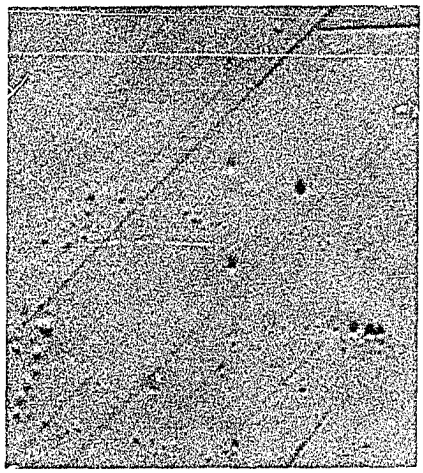

a

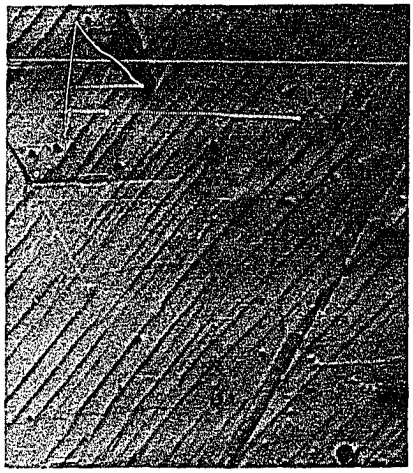

b

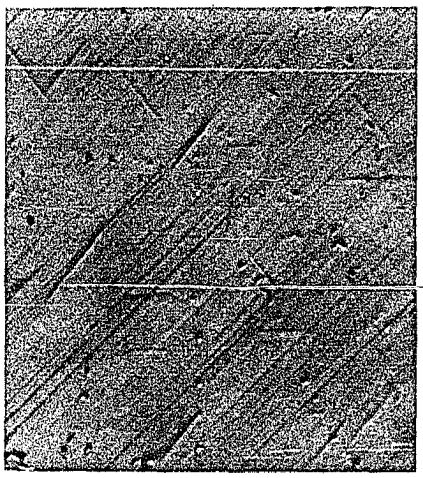

c

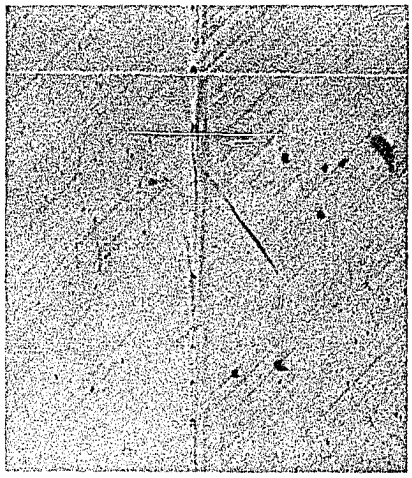

d

moved against the grain boundaries and were more easily absorbed by the tilt boundaries. Since the tilt boundaries were better able to accommodate the dislocations less local stress was exerted on the nucleation sites so that a greater external stress had to be applied to cause nucleation to occur.

IV. SUMMARY AND CONCLUSIONS

Bicrystals of yttrium containing pure <10$\bar{1}$0> twist or pure <11$\bar{2}$0> tilt boundaries were loaded in uniaxial compression to just beyond their yield points. When the critical resolved yield stress was plotted against the degree of twist or tilt misorientation, the strength was found to increase almost linearly at first and then to level off at a plateau of about 5° misorientation. Tilt boundary samples were stronger, with their strength increasing from a single crystal value of 0.34 kg/mm^2 to a plateau value of 0.70 kg/mm^2. This is compared with a plateau value of 0.58 kg/mm^2 for twist boundary samples. The strengthening mechanism in the low angle ($<5^{\circ}$) region appears to have been due to the formation of jogs in the glide and boundary dislocations when the glide dislocations passed through the boundary. The observed strengthening while not as large as the theoretical strengthening accounted for the results quite well when the crude force-distance model used is considered.

The stress plateaus and lack of slip line continuity across the higher angle ($>5^{\circ}$) boundaries indicated that a different strengthening mechanism operated in this region. It must have been associated with the force to nucleate dislocations due to the external stress and the local stress of dislocations in the vicinity of the boundary. Tilt boundaries apparently could relax the stress field of the glide dis-

locations better than twist boundaries so that more external stress was required to nucleate new dislocations near tilt boundaries than twist boundaries.

The deformation modes of yttrium were determined for a variety of loading conditions. Slip occurred primarily on the $\{10\bar{1}0\}\langle 1\bar{2}10\rangle$ system but was forced to occur on the (0001) $\langle 11\bar{2}0\rangle$ system by plane strain compression. The primary twin mode was the $\{11\bar{2}1\}\langle \bar{1}\bar{1}26\rangle$ mode and the secondary twin mode was the $\{10\bar{1}2\}\langle \bar{1}011\rangle$ mode. No deformation modes other than a few $\{11\bar{2}1\}\langle \bar{1}\bar{1}26\rangle$ twins at the ends of the gage length operated in c-axis compression and failure occurred by $\{11\bar{2}3\}$ fracture. This probably accounts for the poor fabricability of yttrium.

Thermal groove studies on the bicrystals provided relative grain boundary energies for yttrium and yielded a theoretical surface energy of 1460 erg/cm^2. The grain boundary energy of yttrium was shown to obey the Read-Shockley theory for small angle dislocation boundaries with $R_0 = -0.98$ and $A = 1.28$.

V. LITERATURE CITED

1. Aston, R. L. The tensile deformation of large aluminum crystals at crystal boundaries. Proc. Cambridge Phil. Soc. 23, 549 (1926).

2. Boas, W. and Hargreaves, M. E. On the inhomogeneity of plastic deformation in the crystals of an aggregate. Proc. Roy. Soc. A 193, 89 (1948).

3. Petch, N. J. The cleavage strength of polycrystals. J. Iron and Steel Inst. 174, 25 (1953).

4. Boas, W. and Ogilvie, G. J. The plastic deformation of a crystal in a polycrystalline aggregate. Acta Met. 2, 655 (1954).

5. Elbaum, C. Plastic deformation of aluminum multicrystals. AIME Trans. 218, 444 (1960).

6. McLean, D. Grain boundaries in metals. London, England, Oxford University Press, 1960.

7. Li, J. C. M. Pile-up of dissociated dislocations and the strength-grain size relationship. Phil. Mag. 19, 189 (1969).

8. Marcinkowski, M. J. and Lipsett, H. A. The plastic deformation of chromium at low temperatures. Acta Met. 10, 95 (1962).

9. Chalmers, B. The influence of the difference of orientation of two crystals on the mechanical effect of their boundary. Proc. Roy. Soc. A 162, 120 (1937).

10. Kawada, T. On the plastic deformation of zinc bicrystals. J. Phys. Soc. Jap. 6, 362 (1951).

11. Gilman, J. J. Deformation of symmetric zinc bicrystals. Acta Met. 1, 426 (1953).

12. Clark, R. and Chalmers, B. Mechanical deformation of aluminum bicrystals. Acta Met. 2, 80 (1954).

13. Aust, K. T. and Chen, N. K. Effect of orientation difference on the plastic deformation of aluminum bicrystals. Acta Met. 2, 632 (1954).

14. Washburn, J. Effect of the structure of dislocation boundaries on yield strength. AIME Trans. 203, 675 (1955).

15. Livingston, J. D. and Chalmers, B. Multiple slip in bicrystal deformation. Acta Met. 5, 322 (1957).

16. Davis, R. S., Fleisher, R. L., Livingston, J. C. and Chalmers, B. Effect of orientation on the plastic deformation of aluminum single crystals and bicrystals. AIME Trans. 209, 136 (1957).

17. Craig, C. and Chalmers, B. Deformation of zinc tricrystals. Can. J. Phys. 35, 38 (1957).

18. Hauser, J. J. and Chalmers, B. The plastic deformation of bicrystals of fcc metals. Acta Met. 9, 802 (1961).

19. Fleisher, R. L. and Backofen, W. A. Effects of grain boundaries in tensile deformation at low temperatures. AIME Trans. 218, 243 (1960).

20. Mote, J. D. and Dorn, J. E. Deformation and fracture of magnesium bicrystals. AIME Trans. 218, 491 (1960).

21. Kratochvi'lova', N. and Sestak, B. Slip propagation over the grain boundaries at plastic deformation of Fe-3% Si alloy. Phys. Stat. Solid 5, 343 (1964).

22. Davis, K. G., Teghtsoonian, E. and Lu, A. Slip band continuity across grain boundaries in aluminum. Acta Met. 14, 1677 (1966).

23. Hook, R. E. and Hirth, J. P. The deformation behavior of isoaxial bicrystals of Fe-3% Si. Acta Met. 15, 535 (1967).

24. Hook, R. E. and Hirth, J. P. The deformation of non-isoaxial bicrystals of Fe-3% Si. Acta Met. 15, 1099 (1967).

25. Reed-Hill, R. E. The role of deformation twinning in the plastic deformation of a polycrystalline anisotropic metal, In Reed-Hill, R. E., Hirth, J. P. and Rodgers, H. C., eds. Deformation twinning. London, England, Gordon and Breach, 1964, pp. 295-301.

26. Boas, W. and Schmid, E. On the deformation of cadmium crystals. Zeit. Phys. 54, 16 (1929).

27. Price, P. B. Nonbasal glide in dislocation free cadmium crystals. J. Appl. Phys. 32, 1746 (1961).

28. Mark, H., Polanyi, M. and Schmid, E. Glide elements of zinc. Zeit. Phys. 12, 58 (1922).

29. Mathewson, C. H. and Phillips, A. J. Twinning in beryllium, magnesium, zinc and cadmium. AIME Trans. 78, 445 (1928).

30. Rosenbaum, H. S. Non-basal slip and twin accomodation in zinc crystals. Acta Met. 9, 742 (1961).

31. Gilman, J. J. Etch pits and dislocations in zinc monocrystals. AIME Trans. 206, 998 (1956).

32. Bell, R. L. and Cahn, R. W. The dynamics of twinning and the interrelation of slip and twinning in zinc crystals. Proc. Roy. Soc. A239, 494 (1957).

33. Price, P. B. Pyramidal glide and the formation and climb of dislocation loops in nearly perfect zinc crystals. Phil. Mag. 5, 873 (1960).

34. Hauser, F. E., Landon, P. R. and Dorn, J. E. Deformation and fracture mechanisms of polycrystalline magnesium at low temperatures. ASM Trans. 48, 986 (1956).

35. Mote, J. D. and Dorn, J. E. Deformation and fracture of magnesium bicrystals. AIME Trans. 218, 491 (1960).

36. Reed-Hill, R. E. and Robertson, W. J. Deformation of magnesium single crystals by non-basal slip. J. Metals 9, 496 (1957).

37. Kelley, E. W. and Hosford, W. F. Plane strain compression of magnesium and magnesium alloy crystals. AIME Trans. 242, 5 (1968).

38. Churchman, A. T. Deformation mechanisms and work hardening in rhenium. AIME Trans. 218, 262 (1960).

39. Tyson, W. R. Slip modes of thallium. Acta Met. 17, 863 (1969).

40. Westlake, D. G. Hydride habit planes and deformation planes of hcp metals. Acta Met. 15, 1407 (1967).

41. Baldwin, D. H. and Reed-Hill, R. E. Some observations of the deformation modes of polycrystalline hafnium and zirconium. AIME Trans. 233, 248 (1965).

42. Rapperport, E. J. Room temperature deformation processes in zirconium. Acta Met. 7, 254 (1959).

43. Rapperport, E. J. and Hartley, C. S. Deformation modes of zirconium at 77°, 575°, and 1075°K. AIME Trans. 218, 869 (1960).

44. Westlake, D. G. Dislocation models of twinning, In Reed-Hill, R. E., Hirth, J. P., and Rodgers, H. C., eds. Deformation twinning. London, England, Gordon and Breach, 1964, pp. 33-42.

45. Liu, T. S. and Steinberg, M. A. Deformation twinning in titanium. J. Metals 4, 1043 (1952).

46. Rosi, F. D., Dube, C. A. and Alexander, B. H. Mechanism of plastic flow in titanium-determination of slip twinning elements. J. Metals 5, 257 (1953).

47. Anderson, E. A., Jillson, D. C. and Dunbar, S. R. Deformation mechanisms in alpha titanium. AIME Trans. 197, 1191 (1953).

48. Rapperport, E. J. and Hartley, C. S. Deformation modes of yttrium at room temperature. AIME Trans. 215, 1071 (1959).

49. Lee, H. T. and Brick, R. M. Deformation of veryllium single crystals at 25 to 500°C. ASM Trans. 48, 1003 (1956).

50. Kaufman, D. F., Pickett, J. J. and Aronin, L. R. Fundamentals of single-crystal deformation in zone-refined beryllium. U.S. Atomic Energy Commission Report NMI-1266 [Nuclear Metals Division of Textron, Inc., West Concord, Mass.]. 1965.

51. Amelinckx, S. and Dekeyser, W. The structure and properties of grain boundaries. Solid State Phys. 8, 393 (1959).

52. Amelinckx, S. The direct observation of dislocations. Solid State Phys. 16, Suppl. 6, 64 (1964).

53. Vogel, F. L. Dislocations in low angle boundaries in germanium. Acta Met. 3, 245 (1955).

54. Schober, T. and Balluffi, R. W. Dislocation sub-boundary arrays in oriented thin-film bicrystals of gold. Phil. Mag. 20, 511 (1969).

55. Schober, T. and Balluffi, R. W. Quantitative observation of misfit dislocation arrays in low and high angle twist grain boundaries. Phil. Mag. 21, 109 (1970).

56. Read, W. T. and Shockley, W. Dislocation models of crystal grain boundaries. Phys. Rev. 78, 275 (1950).

57. Gjostein, N. A. and Rhines, F. N. Absolute interfacial energies of [001[tilt and twist grain boundaries in copper. Acta Met. 7, 319 (1959).

58. Cottrell, A. H. Dislocations and plastic flow in crystals. Oxford, England, Clarendon Press, 1953.

59. Barrett, C. S. An abnormal after-effect in metals. Acta Met. 1, 2 (1953).

60. Jaswon, M. A. and Foreman, A. J. E. The non-hookean interaction of a dislocation with a lattice inhomogeneity. Phil. Mag. 53, 201 (1952).

61. Carrington, W., Hale, K. F. and McLean, D. Arrangement of dislocations in oron. Proc. Roy. Soc. A259, 203 (1960).

62. Haberman, C. E. and Daane, A. H. The preparation and properties of distilled yttrium. U.S. Atomic Energy Commission Report IS-521 [Ames Lab., Ames, Iowa] 1962.

63. Cullity, B. D. Elements of X-ray diffraction. Reading, Mass., Addison-Wesley, 1956.

64. Greninger, A. B. and Troiano, A. R. The mechanism of martensite formation. AIME Trans. 185, 590 (1949).

65. Eshelby, J. D., Read, W. T. and Shockley, W. Anisotropic elasticity with application to dislocation theory. Acta Met. 1, 251 (1953).

66. Foreman, A. J. E. Dislocation energies in anisotropic crystals. Acta Met. 3, 322 (1955).

67. Yoo, M. H. and Wei, C. T. Application of anisotropic elasticity theory to the plastic deformation in hexagonal zinc. Phil. Mag. 13, 759 (1966).

68. Roy, R. B. Application of anisotropic elasticity theory to the choice of primary slip systems in cph metal crystals. Phil. Mag. 15, 477 (1967).

69. Mykura, H. An interferometric study of grain boundary grooves in tin. Acta Met. 3, 436 (1955).

70. Mykura, H. The variation of surface tension of nickel with crystallographic orientation. Acta Met. 9, 570 (1961).

71. Gjostein, N. A. The absolute interfacial energies in [001] tilt and twist grain boundaries in copper. Ph.D. thesis, Carnegie Institute of Technology Library, Pittsburgh, Pa., 1958.

72. Tolman, F. R. and Wood. J. G. Fringe spacing in interference microscopes. J. Sci. Instrum. 33, 236 (1956).

73. Buttner, F. H., Udin, H. and Wulff, J. Surface tension of solid gold. AIME Trans. 191, 1209 (1951).

74. Funk, E. R., Udin, H. and Wulff, J. Surface tension of solid silver. AIME Trans. 191, 1206 (1951).

75. Weertman, J. and Weertman, J. R. Elementary dislocation theory. New York, N.Y., Macmillan Co., 1964.

76. Smith, J. F. and Gjevre, J. A. Elastic constants of yttrium single crystals in the temperature range 4.2-400°K. J. Appl. Phys. 31, 645 (1960).

77. Frank, F. C. and Nicholas, J. F. Stable dislocations in the common crystal lattices. Phil. Mag. 44, 1213 (1953).

78. Peach, M. and Koehler, J. S. The forces exerted on dislocations and the stress fields produced by them. Phys. Rev. 80, 436 (1950).

79. Conrad, H. The cryogenic properties of metals, In High strength materials, Zackary, V. F., ed., New York, N.Y., Wiley, Inc., 1965.

80. Basinski, Z. S. Thermally activated glide in fcc metals and its application to the theory of strain hardening. Phil. Mag. 4, 393 (1959).

81. Conrad, H. Thermally activated deformation of metals. J. Metals 16, 582 (1964).

82. Koepke, B. G., Gibson, E. D. and Scott, T. E. Tensile behavior of polycrystalline yttrium from 77 to 773 K. ASM Trans. 60, 409 (1967).

VI. ACKNOWLEDGMENTS

I would like to thank Dr. T. E. Scott whose extreme patience and excellent advice during the trying times of this investigation were the stimulation needed to solve the problems.

The help of: Mr. C. V. Owen for his advice on experimental techniques, Mr. L. K. Reed for building necessary experimental equipment and preparing samples, Mr. H. H. Baker for advice and services pertaining to metallography, Mr. A. D. Johnson for performing the necessary welding, and Miss Verna Thompson for typing the manuscript, is deeply appreciated.

Finally, I would like to thank Dr. D. T. Peterson for encouraging me to seek this education level and my wife, Janice, for her self sacrifice and moral support during this time span.